

# Effect of planetary boundary layer evolution on new particle formation events over Cyprus

Neha Deot<sup>1</sup>, Vijay P. Kanawade<sup>1,2\*</sup>, Alkistis Papetta<sup>1</sup>, Rima Baalbaki<sup>3,1</sup>, Michael Pikridas<sup>1</sup>, Franco Marenco<sup>1</sup>, Markku Kulmala<sup>3</sup>, Jean Sciare<sup>1</sup>, K. Lehtipalo<sup>3,4</sup>, Tuija Jokinen<sup>1\*</sup>

<sup>1</sup>Climate and Atmosphere Research Center (CARE-C), The Cyprus Institute, Nicosia, Cyprus

<sup>2</sup>Center for Earth, Ocean and Atmospheric Sciences, University of Hyderabad, Hyderabad, India

<sup>3</sup>Institute for Atmospheric and Earth System Research (INAR), University of Helsinki, Helsinki, Finland

<sup>4</sup>Finnish Meteorological Institute, Helsinki, Finland

\*Correspondence: Tuija Jokinen ([t.jokinen@cyi.ac.cy](mailto:t.jokinen@cyi.ac.cy)) and Vijay P. Kanawade ([vijaykanawade03@yahoo.co.in](mailto:vijaykanawade03@yahoo.co.in))

**Keywords:** New particle formation, planetary boundary layer, free troposphere, mountain environments

## Abstract.

Atmospheric new particle formation (NPF) occurs ubiquitously in the atmosphere, but more often in the planetary boundary layer (PBL). However, particle formation and early growth are poorly understood processes in aerosol science, particularly over the Eastern Mediterranean and Middle East (EMME) region, which has been recognised as a global climate change hot spot. Here, we present semi-continuous concurrent measurements of ion and particle size distributions in Cyprus for the year 2022 from a lower-altitude rural background site (Agia Marina Xyliatou, AMX, 532 m a.m.s.l.) and a higher-latitude mountain background site (Troodos, TRO, 1819 m a.m.s.l.) with only about 20 km distance between the sites. We also used concurrent measurements of sulfur dioxide, ozone, and meteorological parameters from both sites. The boundary layer evolution and its impact on the occurrence of NPF events at a mountain site were investigated using a combination of water vapour mixing ratio, a passive tracer of PBL dynamics, at both sites and the Vaisala ceilometer estimated and screened PBL height from AMX. We found that NPF event frequencies are comparable between AMX (60%)

34 and TRO (54%), however only half of the observed NPF events at both sites were observed  
35 concurrently. The smaller mode diameter at AMX than at TRO indicates that NPF was initiated  
36 near AMX. The observed time for the PBL height to reach the TRO altitude relative to the NPF  
37 event start-time at AMX (1.73 hours) is comparable with the time lag between peak particle  
38 number concentrations during concurrent NPF events (1.57 hours). Additionally, the growth  
39 rates of smaller particles (3–7 nm) were similar, while larger particles (7–25 nm) exhibited  
40 higher growth rates at TRO. This suggests that particle growth occurred rapidly in air mass  
41 transported from lower altitudes, likely driven by vertical mixing or up-valley winds. Analysis  
42 of air mass trajectories supports this interpretation, indicating prior contact of air masses with  
43 the PBL before reaching TRO and highlighting the critical role of vertical dynamical mixing  
44 in NPF processes. The TRO site is within the PBL for about 25% of days during late winter  
45 and early spring, increasing to >80% for the rest of the year, which supports our findings. Our  
46 results highlight the significant impact of secondary aerosol production in the evolving PBL  
47 on higher-altitude environments, though the vertical extent of nucleation processes remains  
48 unclear. Understanding these processes is crucial for climate models, as the PBL drives the  
49 exchange of energy, moisture and atmospheric constituents, including aerosols, with the  
50 atmosphere above.

51

## 52 **1. Introduction**

53 Atmospheric new particle formation (NPF) events involve the formation of molecular clusters,  
54 via gas-to-particle conversion, from precursor vapours such as sulfuric acid, ammonia, amines,  
55 oxidation products of volatile organic compounds, and other trace gases that can form low-  
56 volatility complexes, and subsequent growth of these small clusters to larger particles  
57 (Kulmala, 2003; Zhang et al., 2004). Globally, NPF is the largest source of aerosol numbers in  
58 the atmosphere (Kerminen et al., 2012; Wang and Penner, 2009). These newly formed particles  
59 can reach cloud condensation nuclei (CCN) sizes (particle diameter of 50-100 nm and larger)  
60 by coagulation and condensation of additional vapours (Kerminen et al., 2018; Sebastian et al.,  
61 2022; Pierce and Adams, 2009; Westervelt et al., 2013; Williamson et al., 2019). Global  
62 modelling simulations showed that NPF events produce half of the present-day global CCN  
63 number (Merikanto et al., 2009; Spracklen et al., 2008; Westervelt et al., 2014; Yu and Luo,  
64 2009), with an estimated uncertainty range from 38 to 66% (Gordon et al., 2017). The  
65 uncertainty in CCN production in the global climate model itself stems partly from the  
66 uncertainty in particle formation and growth (Ipcc, 2023). Additionally, human exposure to

67 inhalable fine particles, from both primary and secondary sources, has serious health risks that  
68 can lead to premature death (Lelieveld et al., 2019).

69

70 To date, there are a scanty number of studies investigating characteristics of NPF events over  
71 Cyprus (Baalbaki et al., 2021; Brilke et al., 2020; Debevec et al., 2018; Gong et al., 2019) and  
72 overall the limited number of studies over the EMME region (Aktypis et al., 2023; Aktypis et  
73 al., 2024; Dinoi et al., 2023; Hakala et al., 2019; Hussein et al., 2020; Hakala et al., 2023;  
74 Pikridas et al., 2012; Kalkavouras et al., 2019; Kalivitis et al., 2019; Kalkavouras et al., 2020;  
75 Kalkavouras et al., 2021; Manninen et al., 2010). The EMME region is characterised by diverse  
76 air masses originating from continental, maritime, and desert areas, which affect the  
77 atmospheric composition and climate in the area (Bimenyimana et al., 2023; Vrekoussis et al.,  
78 2022; Zittis et al., 2022). While NPF events have been frequently observed in western Saudi  
79 Arabia without any clear seasonal pattern (Hakala et al., 2019), Hussein et al. (2020) observed  
80 the highest NPF event frequency during summer in Amman, Jordan. In contrast, NPF events  
81 were frequently observed during spring and autumn in the eastern Mediterranean (Baalbaki et  
82 al., 2021; Kalivitis et al., 2019). The frequent occurrence of NPF events in the eastern  
83 Mediterranean has been linked to various factors, such as solar radiation/temperature, terrestrial  
84 biogenic activity, higher sulfuric acid (H<sub>2</sub>SO<sub>4</sub>) concentrations, high-dust episodes, and/or air  
85 mass history, but it is still not completely clear what drives the frequent occurrence of NPF  
86 events over this region (Baalbaki et al., 2021). A previous study showed that NPF events  
87 occurred on 58% of days annually at a lower-altitude site, **Agia Marina Xyliatou (AMX)**  
88 (Baalbaki et al., 2021), which is the highest reported frequency after South Africa (86%)  
89 (Hirsikko et al., 2012) and Saudi Arabia (73%) (Hakala et al., 2019). In contrast, NPF events  
90 occurred only on 12% of days during summer at a higher-altitude mountain site (Helmos  
91 mountain at 2314 m a.m.s.l.) in Greece (Aktypis et al., 2024). Previous studies have shown that  
92 NPF events at higher-altitude locations occur under the influence of up-valley winds, which  
93 channel precursor gases to higher altitudes, typically when the boundary layer extends above  
94 the site's altitude (Bianchi et al., 2016; Tröstl et al., 2016a; Sebastian et al., 2021), and NPF  
95 events were observed even at higher vapour condensation sink compared to non-events  
96 (Sellegrì et al., 2019). On the contrary, Boulon et al. (2011) showed that NPF events were  
97 observed more frequently in the free troposphere (43.5% of the total observation days at the  
98 Puy de Dôme station, 1465 m a.m.s.l.) than within the **planetary boundary layer (PBL)** lower-  
99 altitude (2.5% of the total observation days at the Opme station, 660 m a.m.s.l.) in Central  
100 France.

101

102 **Boundary layer NPF phenomena have extensively been studied** worldwide (Nieminen et al.,  
103 2014; Kerminen et al., 2018; Nieminen et al., 2018; Lee et al., 2019; Kulmala et al., 2004),  
104 **although up to which altitude NPF events take place in the PBL, and where they are initiated**  
105 **is still unclear** (Wehner et al., 2010; Stratmann et al., 2003; Minguillón et al., 2015). Minguillón  
106 et al. (2015) demonstrated that intense NPF events in Barcelona primarily occur at a surface  
107 level around midday, coinciding with high insolation and pollution dilution, whereas early-  
108 morning NPF events are constrained to higher altitudes due to the inhibition of these events by  
109 high surface-level condensation sink (CS). Carnerero et al. (2018) demonstrated that ultrafine  
110 particles are formed exclusively inside the mixed layer, and as the mixed layer grows, ultrafine  
111 particles are detected at higher levels within PBL, while Wehner et al. (2010) observed well-  
112 mixed ultrafine particles (5-10 nm) throughout the PBL. A one-dimensional coupled column  
113 model, SOM-TOMAS (Statistical Oxidation Model of organic chemistry and Two Moment  
114 Aerosol Sectional microphysics model), demonstrated that enhanced NPF rates in the upper  
115 mixed layer are strongly influenced by temperature, vertical mixing, and gas-phase precursor  
116 concentrations (O'donnell et al., 2023). **Aircraft observations over boreal forests showed that**  
117 **particle concentrations (>1.5 nm) peak near the surface in the morning and mix within the**  
118 **evolving PBL layer during the day (Leino et al., 2019). However, airborne observations are**  
119 **costly and operationally challenging. Our sites offer a unique opportunity to study the vertical**  
120 **extent of NPF events and aerosol populations within the PBL, due to their close proximity, and**  
121 **the mountain background site (TRO) is within the PBL for about >80% of days during the year.**  
122 **The intense solar radiation, the intricate mixture of both natural and anthropogenic emissions**  
123 **from continental and marine origins, the presence of local breeze systems (mountain, valley,**  
124 **sea, and land) and elevated dust layers further add complexity to the PBL–NPF relationship**  
125 **over the region. The combination of these factors poses a significant challenge in understanding**  
126 **the drivers behind the frequent NPF events observed in Cyprus and, more broadly, across the**  
127 **Eastern Mediterranean.**

128

129 In this work, we used semi-continuous concurrent measurements of ion and particle size  
130 distributions for the year 2022 from a lower-altitude rural background site (AMX) and a higher-  
131 **altitude** mountain background site (TRO) in Cyprus with a 1287 m difference in altitude in 20  
132 km distance between the observational sites. **We present analysis on concurrent and individual**  
133 **(i.e. an event happening only at one site while the other site did not show an event) NPF events.**

134 The main aim is to examine the effect of PBL evolution on NPF events at a background  
135 mountain site in Cyprus.

136

## 137 **2. Materials and methods**

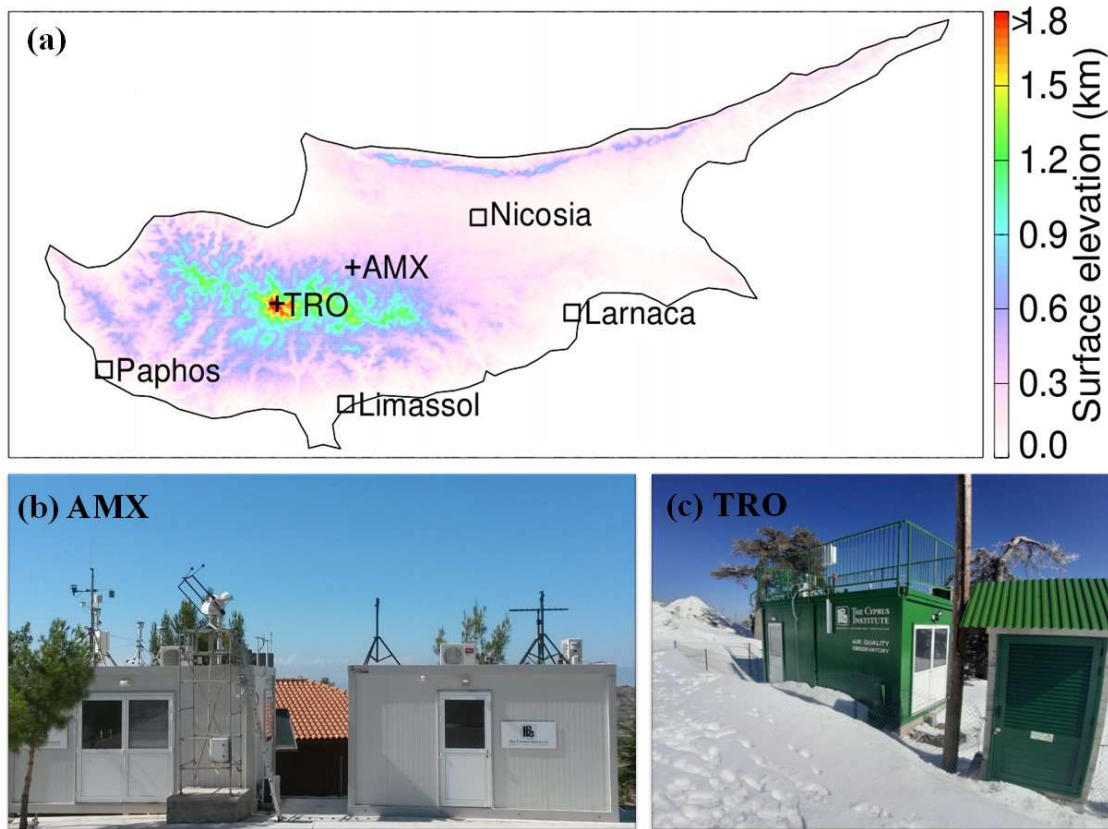
### 138 **2.1 Measurement Sites**

139 The Eastern Mediterranean and Middle East region has been recognized as a global climate  
140 change hotspot, which serves as a convergence zone for air masses originating from three  
141 distinct continents (Europe, Asia, and North Africa), including marine, anthropogenic, and  
142 desert dust sources. AMX and TRO are sites of the Cyprus Atmospheric Observatory (CAO)  
143 network, operated by the Climate and Atmosphere Research Center (CARE-C) of the Cyprus  
144 Institute. The AMX site (35.038692° N, 33.057850° E) is located at 532 m a.m.s.l. between two  
145 villages, Agia Marina Xyliatou and Xyliatos, at the foothills of the Troodos mountain range in  
146 the central Republic of Cyprus. The AMX site is located about 1.5 km South of Agia Marina  
147 Xyliatou and about 2.2 km Northeast of Xyliatos. The AMX site hosts instruments affiliated  
148 with several research infrastructures such as the cooperative program for monitoring and  
149 evaluation of the long-range transmission of air pollutants in Europe (referred to as the  
150 European Monitoring and Evaluation Programme, EMEP), the air quality network of Cyprus  
151 operated by the Department of Labour Inspection (DLI), regional Global Atmospheric Watch  
152 (GAW) program of the World Meteorological Organization (WMO), the Aerosols, Clouds and  
153 Trace Gases Research Infrastructure (ACTRIS) aerosol in situ network, e-Profile (part of  
154 EUMETNET), and NASA's AERosol RObotic NETwork (AERONET). Anthropogenic  
155 emissions in the vicinity of the AMX site are minimal and the major cities are located at about  
156 35 km (Nicosia) to the Northeast and about 50 km (Larnaca) to the Southeast.

157

158 The TRO site (34.9430333° N, 32.8654729 E) is located at 1819 m a.m.s.l., close to Mount  
159 Olympus (the highest peak of Cyprus, 1952 m a.m.s.l.) and experiences free tropospheric  
160 conditions, primarily during winter. TRO site may also experience light to moderate snowfall  
161 during winter, usually in January and February, and it is in cloud sporadically. The site is  
162 considered a background higher-altitude mountain location as it has little or no influence from  
163 local anthropogenic activities, except occasional camping or campfire activities in the vicinity  
164 and the staging post for helicopter operations. Small villages such as Prodromos, Palaiomylos,  
165 and Agios Dimitrios are located to the West of the TRO site, while the Troodos village is  
166 located to the Southeast within a 5 km distance. It is located centrally with respect to the major  
167 cities: Limassol, about 36 km to the South, Paphos, 42 km to the Southwest, Nicosia, 50 km to

168 the Northeast, and Larnaca, 70 km to the Southeast. Figure 1 shows the surface elevation map  
169 of Cyprus depicting the locations of AMX and TRO sites and pictures of the AMX and TRO  
170 site premises.  
171



172

173 **Figure 1.** (a) Surface elevation map of Cyprus, including the location of AMX and TRO  
174 observational sites and the major cities. Elevation data is obtained from the U.S. Geological  
175 Survey global digital elevation model (DEM) with a horizontal grid spacing of 30 arc seconds  
176 (approximately 1 km (GTOPO30)). (b) and (c) show AMX and TRO site premises pictures,  
177 respectively.

178

## 179 2.2 Instrumentation

### 180 2.2.1 Neutral Cluster and Air Ion Spectrometer (NAIS)

181 The ion and total particle number size distributions were measured using the NAIS (Airel Ltd.  
182 Estonia) at both measurement sites to detect and characterise NPF events. The NAIS measures  
183 the number size distribution of ions and naturally charged particles in the diameter range of 0.8  
184 – 42 nm for NTP conditions (mobility range:  $3.162 - 0.0013 \text{ cm}^2 \text{ V}^{-1} \text{ s}^{-1}$ ) (Mäkelä et al., 1996),  
185 simultaneously in both positive and negative polarity (Manninen et al., 2016; Mirme and

186 Mirme, 2013). Additionally, the NAIS can measure the total particle size distribution by using  
187 corona charging. Briefly, the NAIS has two parallel cylindrical differential mobility analysers  
188 (DMAs): one classifies positively charged ions, and the other classifies negatively charged  
189 ions. The air is sampled at a flow rate of  $54 \text{ L min}^{-1}$ , with a sampling tube inner diameter of 30  
190 mm and a length of 65 cm. Subsequently, the airflow is divided equally for each polarity before  
191 entering the preconditioning unit. Here, depending on the operational mode, the aerosol  
192 samples either pass through without modification (ion mode), or they are charged to the same  
193 polarity of the analysers (particle mode) or they are charged to the opposite polarity of the  
194 analyser (offset mode). The air sample then reaches the analysers, where it is size-classified in  
195 an electrical field and detected by electrometers. The total particle concentration below  $\sim 2 \text{ nm}$   
196 cannot be detected due to the ions produced by the corona charger itself, and therefore  
197 discarded in the data analyses. The NAIS SPECTOPS software with an instrument-specific  
198 algorithm was used to invert the raw counts into a size distribution. The inverted data was  
199 subsequently corrected for line losses using the Gormley and Kennedy equation for inlet line  
200 losses for laminar flow (Gormley and Kennedy, 1949). **Note that NAIS data is available for**  
201 **approximately 60% and 63% of the days at AMX and TRO, respectively (Fig. S1), which is**  
202 **statistically robust for this analysis.**

203

### 204 **2.2.2 Ceilometer CL51**

205 The Vaisala Ceilometer CL51 is part of the E-PROFILE network, operational since 2021  
206 which coordinates the measurements of vertical profiles of wind, aerosol, and clouds from  
207 radars, lidars, and ceilometers from a network of locations across Europe and provides the data  
208 to the end users. The Vaisala Ceilometer CL51 utilises an eye-safe indium gallium arsenic  
209 (InGaAs) diode-laser lidar technology, emitting 110 ns-long pulses with a wavelength of  
210  $910 \pm 10 \text{ nm}$  and a repetition rate of 6.5 kHz in a vertical or near-vertical direction (Münkel and  
211 Roininen, 2010). The CL51 can measure aerosols and clouds from above the overlap region  
212  $\sim 300 \text{ m}$  up to 15 km nominally, with a vertical resolution of 10 m. The backscatter profile is  
213 used to identify up to three aerosol-layer heights using the gradient method in the  
214 postprocessing software provided by the manufacturer (BL-VIEW), which includes an  
215 automated mixing height detection algorithm described by Emeis et al. (2007). The VAISALA  
216 BL-VIEW software features a “cloud and precipitation filter” known as the enhanced gradient  
217 method (Münkel and Roininen, 2010), which filters out high backscatter signals from clouds  
218 and precipitation before applying the gradient method. BL-View’s calculation is based on the  
219 combined gradient and idealised backscatter methods that enable reliable automatic estimation

220 of the PBL height (PBLH) at a temporal resolution of 16 seconds and a vertical resolution of  
221 10 m. Here, we used Level 3 boundary layer height data with a quality control index of “good”  
222 only.

223

### 224 **2.2.3 Ancillary measurements**

225 We used aerosol optical depth (AOD) and angstrom exponent (AE) data from the AERONET  
226 sunphotometers at both AMX and TRO sites. Trace gas concentrations, such as sulfur dioxide  
227 (SO<sub>2</sub>) and ozone (O<sub>3</sub>), and the meteorological parameters (temperature, relative humidity, solar  
228 radiation, wind speed, and wind direction) at AMX station were taken from the air quality  
229 network of Cyprus operated by the DLI. At the TRO site, TELEDYNE gas analysers for SO<sub>2</sub>  
230 (Model T100U) and O<sub>3</sub> (Model T400) were deployed and meteorological parameters were  
231 obtained from the Department of Meteorology automatic weather station, located about 3.3 km  
232 south of the measurement site. Note that all data is reported in Universal Time Coordinated  
233 (UTC). Local time in Cyprus is UTC+2 from late October to late March (Eastern European  
234 Time) and UTC+3 from late March to late October during daylight saving time (Eastern  
235 European Summer Time). **We have used quality-assured and quality-controlled data using  
236 standard procedures and instrument data quality flags.**

237

### 238 **2.3 Tracers used to investigate PBL evolution**

239 **We used two distinct methods to investigate how often the mountain background site, TRO, is  
240 influenced by PBL evolution.** First, the water vapour mixing ratio (WVMR) at TRO was used  
241 to distinguish between free tropospheric and PBL air. A threshold WVMR value of 5.25 g/kg  
242 **(which is the 30<sup>th</sup> percentile** value of WVMR at the AMX site) was used, with WVMR values  
243 below 5.25 g/kg indicating free tropospheric air (Zha et al., 2023). WVMR was calculated as  
244 follows:

245

$$246 \quad WVMR = B \times \frac{e}{p - e} \quad (1)$$

247

248 where B is a constant (621.9907 g kg<sup>-1</sup>, molecular weight ratio of water to dry air), e and p are  
249 the water vapour pressure and the atmospheric pressure, respectively. e was calculated using  
250 ambient temperature, RH, and pressure (Buck, 1981).

251



252 Secondly, the Vaisala ceilometer estimated PBLH from the AMX site was used to examine the  
253 PBL evolution up to the altitude of the TRO site. The PBLH estimation algorithm might be  
254 influenced by boundary layer stability, near-surface or elevated aerosol layers, moving cloud  
255 systems in the vicinity of the measurement site, and surface type. Zhang et al. (2022) showed  
256 that the ceilometer estimated PBLH generally compares well with the bulk Richardson number  
257 method under stable conditions. ERA5 also used the bulk Richardson number method to  
258 calculate PBLH (Hersbach et al., 2020). Therefore, we apply a robust data filtering technique  
259 to remove under or over-estimated PBLH data values in conjunction with ERA5 PBLH data  
260 (Hersbach et al., 2023), the latest version of ECMWRF reanalysis, which is available on a 1440  
261  $\times$  721 longitude and latitude grid, with a spatial resolution of  $0.25^\circ \times 0.25^\circ$  and a temporal  
262 resolution of 1 hour. First, we remove ceilometer estimated PBLH which is lower or greater  
263 than three standard deviations of PBLH for a given day. Second, we used ERA5 PBLH to  
264 match the diurnal pattern and considered only those days when the correlation coefficient  
265 between ERA5 and Ceilometer PBLH was greater than 0.5 at a statistical significance level of  
266 95%. After applying these constraints, we retained 5688 hourly data points from a total of 7248  
267 valid hourly data points, thereby ensuring that only the most reliable data were included in the  
268 PBLH analysis.

269

## 270 **2.4 Event classification**

271 The traditional ways to classify the given day into different types of NPF events (Dal Maso et  
272 al., 2005; Hirsikko et al., 2007; Kulmala et al., 2012; Manninen et al., 2010) are mainly based  
273 on the visual appearance of a contour plot of particle number size distributions. A day with the  
274 appearance of a new particle mode followed by its growth is identified as an NPF event day  
275 and such events occur over a spatial scale of a few 100's kilometres and a temporal scale of 1-  
276 2 days and are thus referred to as regional NPF events. The downside of these methods is a  
277 large fraction of unclear days, which could be caused by more local NPF events, changes in air  
278 masses, or varying weather conditions. Such unclear events can also be further classified into  
279 different sub-classes (nucleation-mode peak, Aitken-mode, and tail), but it requires additional  
280 information on trace gases and aerosol characteristics (Kanawade et al., 2014; Buenrostro  
281 Mazon et al., 2009). However, the data analysis becomes more complex when these unclear  
282 days form a large fraction of all the days. In addition, these methods omit potentially low-  
283 intensity NPF events such as local or short-lived NPF events (Kulmala et al., 2024). Here, we  
284 used the traditional methodology for classifying a given day into NPF event, non-event and  
285 unclear. Given the asynchronous data gaps in NAIS measurements at both sites, we introduced

286 an additional category labelled 'nodata,' which must be considered when comparing the  
287 frequency of occurrence of different event types. nodata days include the unavailability of the  
288 instrument, maintenance (mainly the cleaning of the instrument during the summer and dust  
289 episodes), troubleshooting of the instrument, and infrequent power cuts at the measurement  
290 site. We present the frequency of occurrence for all these event types and utilise only NPF  
291 events for data analysis in this work.

292

## 293 **2.5 Air mass history analysis**

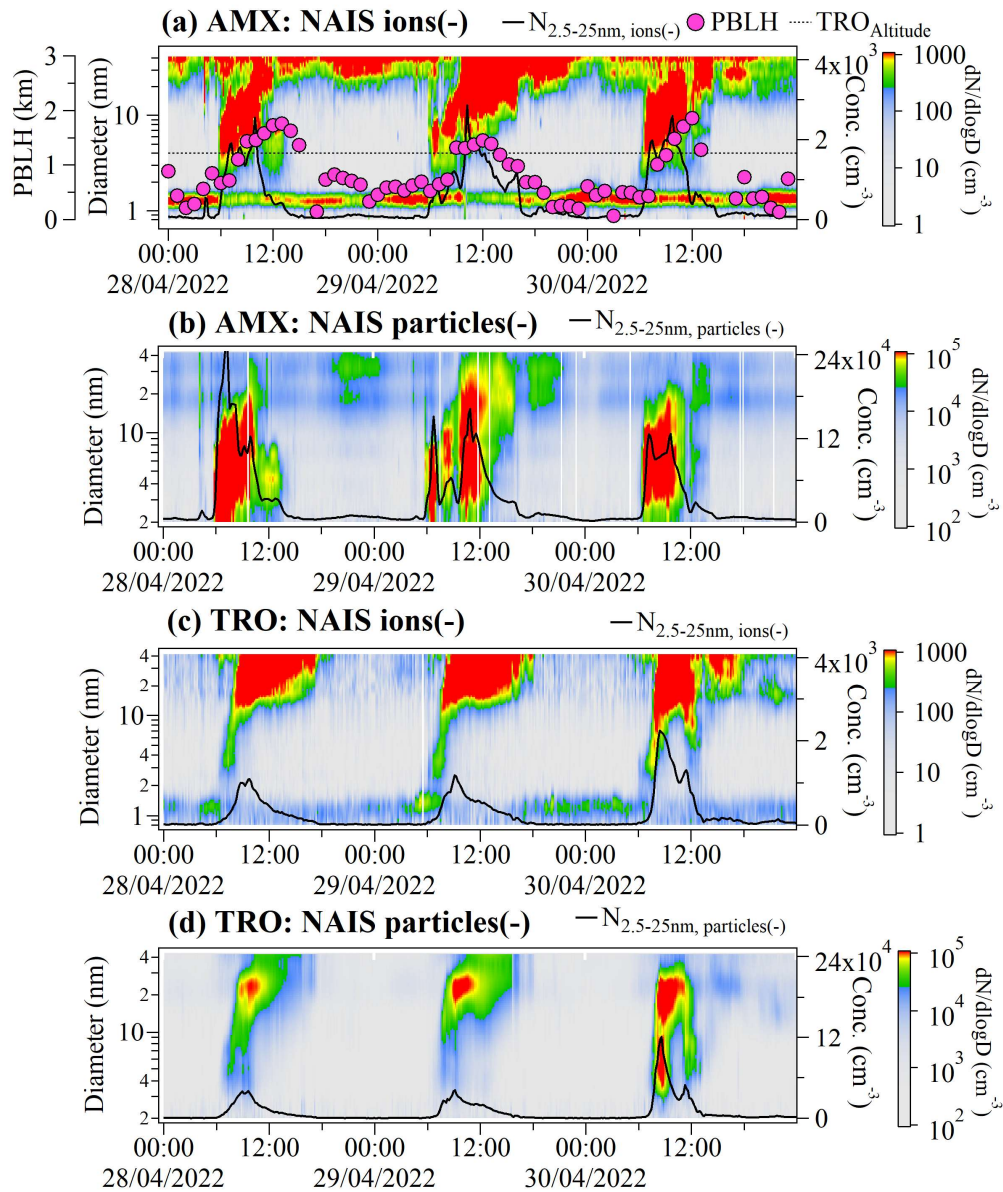
294 Three-day backward air mass trajectories arriving at 1000 m a.m.s.l. and 2000 m a.m.s.l. to  
295 AMX and TRO, respectively, during 6 - 12 UTC were determined using the National Oceanic  
296 and Atmospheric Administration (NOAA) ARL PC-version HYbrid SingleParticle Lagrangian  
297 Integrated Trajectory (HYSPLIT) transport and dispersion model (Draxler and Rolph, 2010),  
298 using 0.25 degree gridded wind fields from the Global Forecast System (GFS).

299

## 300 **3 Results and Discussion**

### 301 **3.1 NPF event frequency and characteristics**

302 The temporal evolution of **negative** ion and particle number size distributions at both sites  
303 (AMX and TRO) for the year 2022 are shown in Fig S1. Ion and particle number concentrations  
304 are generally higher at AMX than at TRO. Figure 2 shows the concurrent evolution of **negative**  
305 ion and particle number size distributions and number concentrations for observed typical NPF  
306 events at both sites and PBLH at the AMX site from 28 - 30 April 2022. The negative ion and  
307 particle number concentrations are two-fold higher at the AMX site as compared to the TRO  
308 site. While larger diameter background particles were continuously present at the AMX site,  
309 they were absent at the TRO site, suggesting that NPF events may be the major source of larger  
310 diameter particles in the Aitken mode at the TRO site (Fig. 2 and S1). Furthermore, the banana-  
311 shaped aerosol formation and growth pattern were significantly broader below 10 nm at the  
312 AMX site compared to the TRO site, suggesting that the intense NPF most likely lasted longer  
313 and the precursor vapour supply was sustained for a longer duration at AMX than at TRO. The  
314 PBLH was higher than the altitude of the TRO site, possibly indicating that the concurrent  
315 occurrence of NPF events at TRO was influenced by the evolution of the PBL (see section 3.3).



316

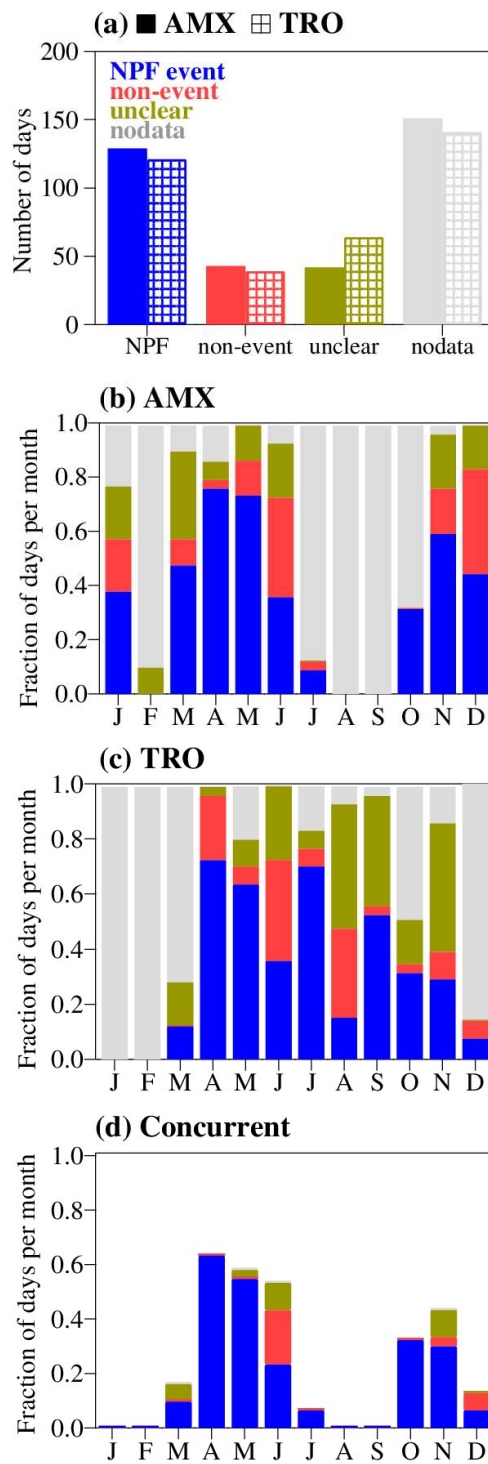
317 **Figure 2.** Time evolution of 10-minute averaged number size distributions of **negative** polarity  
 318 ions and total particles at AMX (a, b) and TRO (c, d), respectively, measured with NAIS from  
 319 28 April to 30 April 2022. The ion and particle number concentrations in the mobility diameter  
 320 range from 2.5 to 25 nm are shown by a solid black line. The PBLH at AMX above the ground  
 321 and the altitude of the TRO site above AMX are indicated by magenta colour dots and a black  
 322 colour dotted line, respectively.

323

324 Figure 3a shows the occurrence frequency of different types of event days at both AMX and  
 325 TRO sites. At AMX, NPF events were observed on 129 days (35.34%), 43 days did not have  
 326 signs of NPF (non-events, 11.78%), while 42 days (11.51%) were unclear and there were no  
 327 valid measurements on 151 days (41.37%) during the calendar year of 2022. At TRO, NPF

328 events were observed on 121 days (33.16%), 39 days did not show NPF (non-events, 10.68%),  
329 64 days were unclear (17.53%), and there were no valid measurements on 141 days (38.63%).  
330 Out of the total observed NPF events at AMX (129 days out of 214 valid observation days,  
331 60%) and at TRO (121 days out of 224 valid observation days, 54%), NPF events  
332 were observed concurrently on 69 days at both sites (Table S1), indicating that the remaining  
333 NPF events occur in different air masses at these sites even with the close proximity of sites  
334 (approximately 20 km). The NPF frequency at the AMX site was the highest during spring as  
335 compared to the rest of the year, analogous to the previous study at AMX (Baalbaki et al.,  
336 2021) and other closest Eastern Mediterranean site, Finokalia atmospheric observation station,  
337 in Crete (Kalivitis et al., 2019). The NPF frequency at the TRO site appears to be the highest  
338 during spring, although the NPF frequency in July was comparable. The gaps in observational  
339 data limit a detailed discussion of the seasonal characteristics of NPF events at both sites,  
340 however, the concurrent observations, covering over 60% at both sites, are sufficient to assess  
341 the impact of PBL evolution on NPF events at the TRO site.

342



343

344 **Figure 3.** (a) Number of days of different event types at both AMX and TRO sites, (b)  
 345 occurrence frequency (in fraction of days per month calculated as the number of event days  
 346 divided by the total number of calendar days in the month) of different event types at AMX,  
 347 (c) same as (b) but for TRO, and (d) same as (b) but for concurrent days of NPF events, non-  
 348 events and unclear days at both AMX and TRO sites, excludes individual different events types  
 349 and nodata.

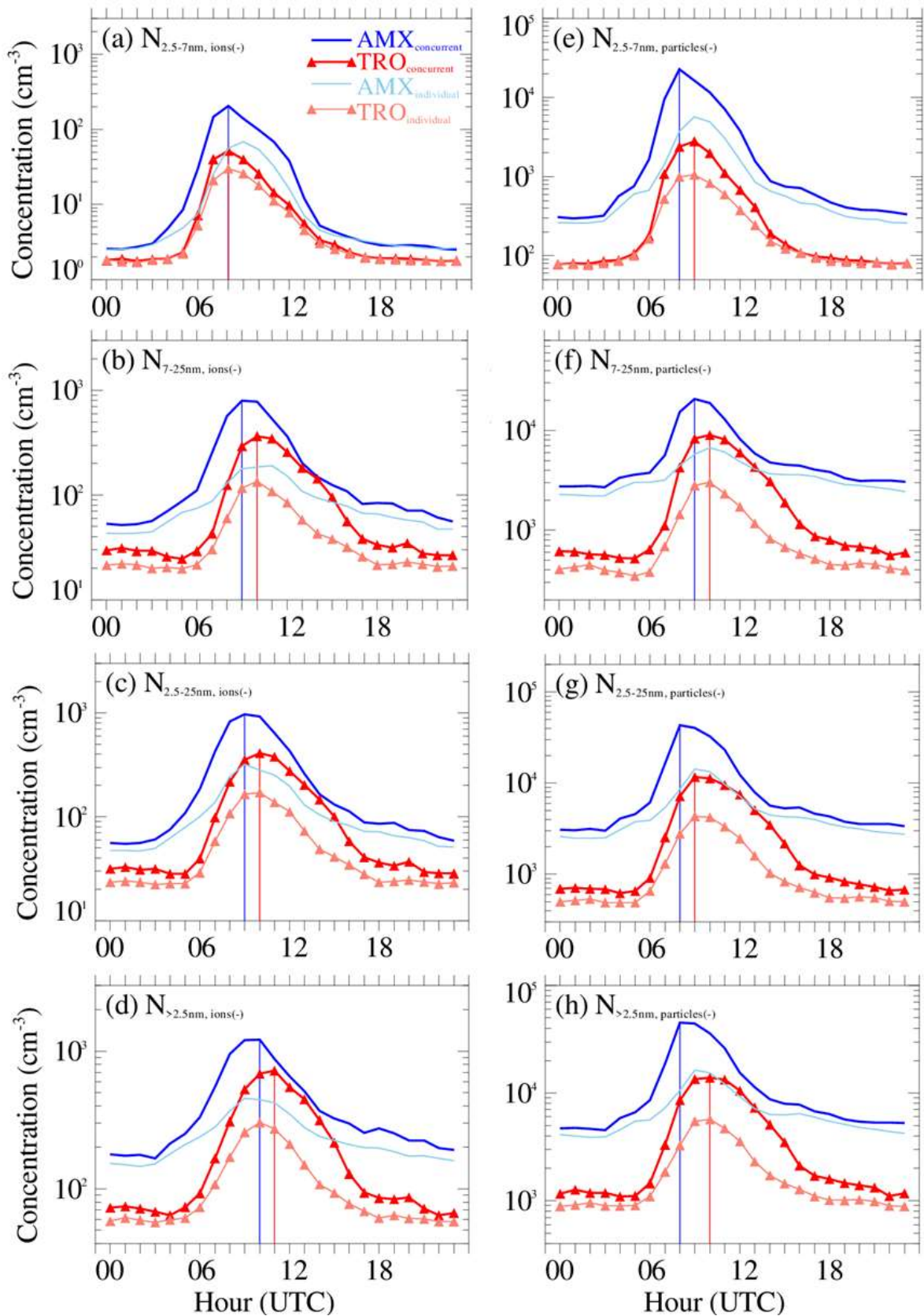
350

### 351 **3.2 Diurnal variation in **negative** polarity size-segregated ion and total particle number** 352 **concentrations, NPF events start-time and mode diameter**

353 Figure 4 shows the diurnal variation of size-segregated ion and particle number concentrations  
354 for **negative** polarity (see Fig. S2 for **positive** polarity) for concurrent NPF events observed at  
355 both sites as well as NPF events observed individually at each site. We used four size classes:  
356 2.5-7 nm, 7-25 nm, 2.5-25 nm, and >2.5 nm for both ions and particles. Ion and particle number  
357 concentrations exhibit similar diurnal cycles, with the highest concentrations occurring  
358 between 06:00 and 14:00 UTC, as NPF is predominately a daytime phenomenon driven by  
359 photochemistry in the presence of solar radiation (Asmi et al., 2011; Jokinen et al., 2017;  
360 Kanawade et al., 2012; Kerminen et al., 2018; Z. Wu et al., 2007). The noontime peak in size-  
361 segregated ion and particle number concentrations indicates the importance of photochemistry  
362 for NPF events at AMX and TRO sites. The concurrent peaks in temperature (Fig. S3a), solar  
363 radiation (Fig. S3b) and sulfur dioxide (Fig. S3c) during NPF events are also visible. The low  
364 relative humidity (Fig. S3d), higher ozone concentrations (Fig. S3e), and lower wind speed  
365 (Fig. S3f) further indicate environmentally favourable conditions to promote particle formation  
366 and growth. **Seasonally averaged diurnal patterns of columnar aerosols (AOD) during spring,**  
367 **summer and autumn closely resemble one another (probably indicating that TRO is influenced**  
368 **by the PBL evolution) with higher aerosol loading at AMX compared to TRO (Fig. S4a),**  
369 **whereas they do not align well in winter (TRO is weakly influenced by the PBL evolution).**  
370 **Additionally, the higher Ångström exponent at TRO (Fig. S4b), particularly in winter when the**  
371 **TRO mostly lies in the free troposphere (see section 3.3), suggests that these small particles**  
372 **are likely from local primary emissions (traffic, residential, etc.) or airborne secondary**  
373 **production or both.** Furthermore, the absence of traffic-induced morning and evening peaks in  
374 size-segregated ion and particle number concentrations suggests that both sites are not  
375 influenced by local traffic emissions (Fig. 4). The blue and red vertical lines in Figure 4 indicate  
376 the occurrence times of peak concentrations for concurrent NPF events at AMX and TRO,  
377 respectively. The peak was consistently shifted to the right at the TRO site, except for  
378 intermediate ions (2.5–7 nm). This shift suggests a temporal delay of NPF events compared to  
379 AMX. This variation could reflect differences in local atmospheric dynamics, such as PBL  
380 evolution alongside aerosol precursors required for aerosol formation and growth. When  
381 mountain sites experience daytime evolution of the PBL, a similar diurnal cycle of aerosol  
382 properties, to that of lower-altitude sites, is typically observed (Collaud Coen et al., 2018).  
383 Therefore, we hypothesise that the NPF event is detected earlier at the AMX site, shortly after

384 sunrise, coinciding with an increase in temperature that drives the evolution of the PBL up to  
385 the height of the TRO site. The evolution of the PBL may carry precursor gases and aerosols  
386 up to the TRO site altitude, resulting in a later starting time of NPF events there.

387



388

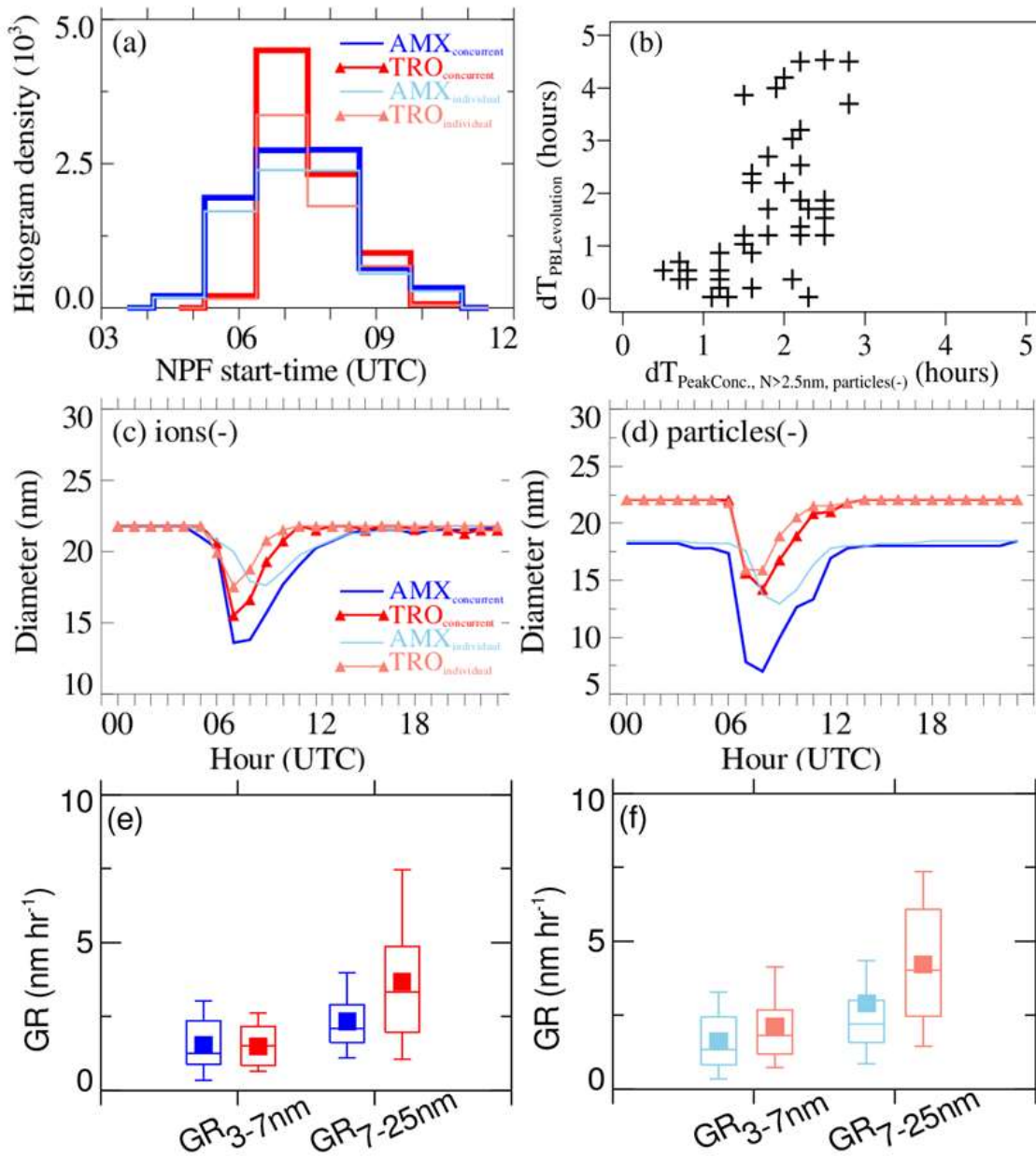
389 **Figure 4.** Median diurnal variation of **negative** polarity ion (a-d) and particle (e-h) size-  
 390 segregated (2.5 - 7 nm, 7 - 25 nm, 2.5 - 25 nm, and >2.5 nm) number concentrations observed  
 391 on concurrent NPF events at AMX (dark blue thick line) and TRO (dark red thick line). The



392 light blue and light red lines are for NPF events observed individually at AMX and TRO,  
393 respectively. The blue and red vertical lines indicate the times at which the peak concentrations  
394 for concurrent NPF events were observed at AMX and TRO, respectively.

395

396 The peak in size-segregated ion and particle number concentrations exhibited a time lag of 1-  
397 2 hours for concurrent NPF events at both sites (Fig. 4). Further, the size-segregated ion and  
398 particle number concentrations were higher at AMX than at TRO. To substantiate our  
399 hypothesis, we first obtained NPF event start-times at both sites. The histogram of NPF event  
400 start-times indicates that NPF events at the TRO site were consistently detected with a time lag  
401 of 1-2 hours compared to AMX (Fig. 5a). We further calculated the time required for the PBL  
402 height to reach the TRO altitude relative to the NPF event start-time at AMX ( $dT_{PBL\text{evolution}}$ )  
403 and the time lag between peak number concentrations of negative polarity particles  $>2.5$  nm  
404 ( $dT_{\text{PeakConc., } N>2.5 \text{ nm, particles(-)}}$ ) for observed concurrent NPF events. Out of 69 concurrent event  
405 days, PBL height data was screened out for 24 days (as explained in section 2.3), leaving 45  
406 data points. The average time lags based on particles and PBL measurements are 1.57 hours  
407 ( $\sim 94$  minutes) and 1.73 hours ( $\sim 104$  minutes), respectively (Fig. 5b). The mode diameter of  
408 negative polarity particles was also larger at TRO than at AMX. At 7:00 UTC, the negative  
409 polarity ion (particle) mode diameters at AMX and TRO were about 13.6 nm (7.8 nm) and 15.5  
410 nm (15.7 nm), respectively (Figs. 5c, 5d). Considering the time lag of 2 hours between these  
411 sites, the negative polarity particle growth rate is estimated to be  $\sim 3.9$  nm  $\text{hr}^{-1}$ . The mode  
412 diameter of positive polarity particles also showed similar behaviour (Fig. S5a, S5b). During  
413 the concurrent NPF event days, the calculated size-segregated growth rates varied from 0.1 to  
414 3.64 nm  $\text{hr}^{-1}$  (3-7 nm) and 0.18 to 6.08 nm  $\text{hr}^{-1}$  (7-25 nm) with a mean and standard deviation  
415 of  $1.53 \pm 0.98$  nm  $\text{hr}^{-1}$  and  $2.35 \pm 1.16$  nm  $\text{hr}^{-1}$ , respectively, at AMX while they varied from 0.12  
416 to 2.91 nm  $\text{hr}^{-1}$  (3-7 nm) and 0.4 to 8.7 nm  $\text{hr}^{-1}$  (7 – 25 nm) with a mean and standard deviation  
417 of  $1.49 \pm 0.71$  nm  $\text{hr}^{-1}$  and  $3.68 \pm 2.22$  nm  $\text{hr}^{-1}$ , respectively, at TRO. The growth rates of smaller  
418 particles (3-7 nm) were similar while the growth rates of larger particles (7-25 nm) were higher  
419 at TRO indicating that the particles grew rapidly during upward airmass transport from AMX  
420 to TRO due to PBL evolution (see section 3.3, Fig. 7), possibly by valley winds or vertical  
421 mixing, on concurrent event days. The size-segregated particle growth rates for positive  
422 polarity also showed similar behaviour (Fig. S5c and S5d). The lower number concentrations  
423 of nucleation mode particles at TRO than at AMX (Fig. 4) can facilitate more availability of  
424 vapour for rapid growth at TRO. Therefore, we next examine PBL evolution and its influence  
425 on the TRO mountain site.



426

427 **Figure 5.** (a) Histogram density of NPF events start-time for the observed concurrent NPF  
 428 events at AMX (dark blue) and TRO (dark red). The light blue and light red coloured lines  
 429 indicate NPF events observed individually at AMX and TRO, respectively. (b) scatter plot of  
 430 the time lag between peak number concentrations of negative polarity particles >2.5 nm  
 431 ( $dT_{\text{PeakConc., N>2.5 nm, particles(-)}$ ) and the time needed for PBL to reach TRO altitude relative to the  
 432 NPF start-time at AMX ( $dT_{\text{PBLEvolution}}$ ). Median diurnal variation of negative polarity (c) ion  
 433 and (d) particle mode diameter. The box-whisker plot of size-segregated particle growth rates  
 434 for negative polarity for the observed (e) concurrent NPF events and (f) individual NPF events.  
 435 The filled square indicates the mean, the horizontal line indicates the median, the bottom and

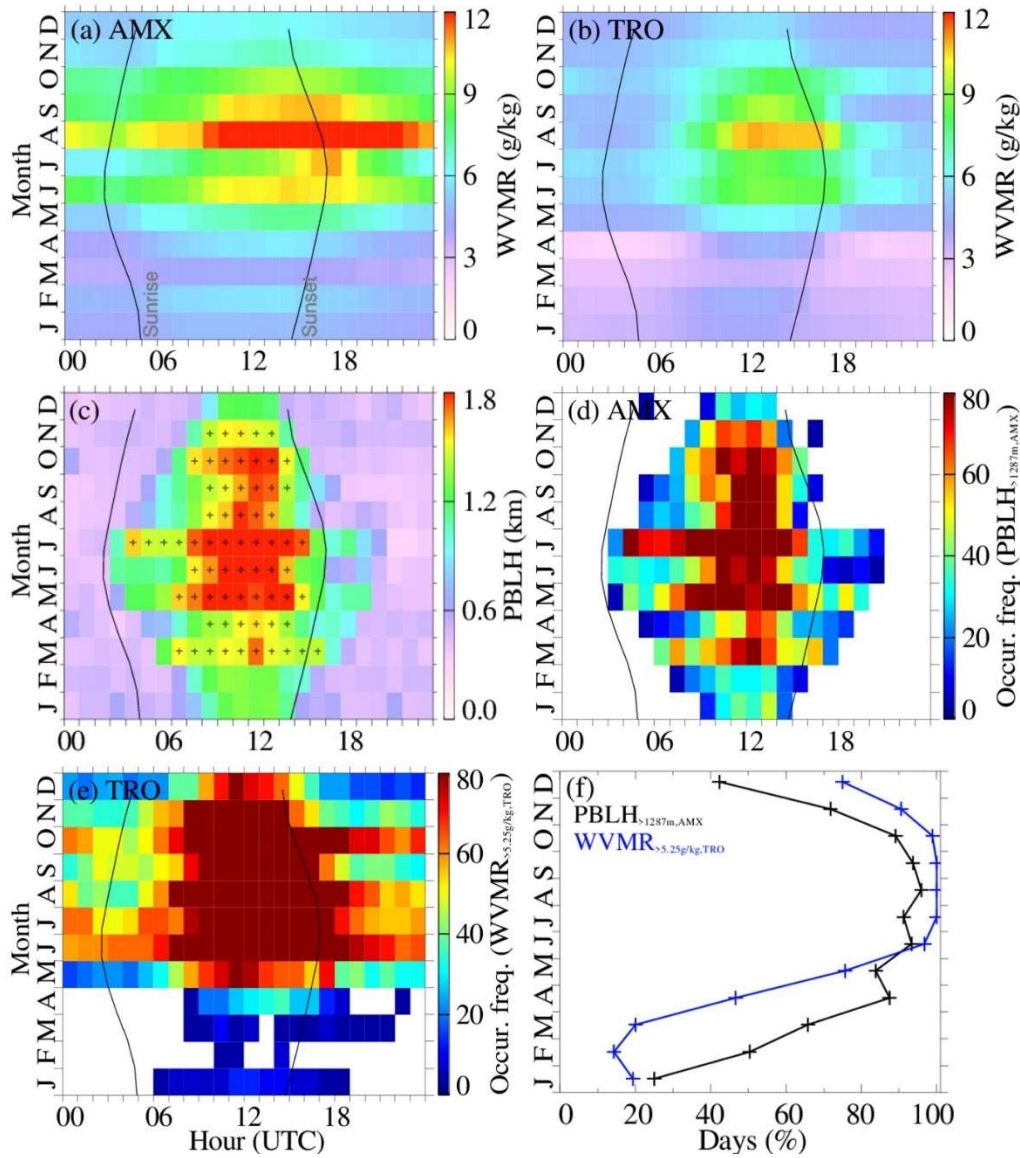
436 top of the box indicate the 25<sup>th</sup> and 75<sup>th</sup> percentiles and the bottom and top of the whisker  
437 indicate the 10<sup>th</sup> and 90<sup>th</sup> percentiles.

438

### 439 **3.3 Examining PBL evolution and its influence on the TRO site**

440 The vertical evolution of the PBL significantly influences meteorological and environmental  
441 factors, such as near-surface pollutant concentrations, wind velocity, and turbulent exchange  
442 of momentum, heat, and moisture (Stull, 1988). The most accurate and common measurements  
443 of thermodynamic profiles are achieved using radiosondes, but the temporal resolution is too  
444 sparse to detect the evolution of the diurnal structure of PBL. Ground-based remote sensing  
445 techniques fill this gap, providing high temporal resolution information, such as sound  
446 detection and ranging (SODAR), radio acoustic sounding system (RASS), and light detecting  
447 and ranging (LiDAR) (Kotthaus et al., 2023). Here, we used ceilometer measurements from a  
448 lower-altitude site (AMX) along with WVMR, passive tracers of PBL dynamics, from both  
449 sites to examine the diurnal evolution of the PBL and assess its impact on the mountain site  
450 (TRO). Figure 6 shows the monthly median diurnal variation of WVMR at both sites, PBLH  
451 at AMX, and the estimates for the influence of the PBL evolution on the TRO site. The monthly  
452 median diurnal variation of WVMR illustrates the probable mixing of air between the lower-  
453 altitude AMX site and the mountain TRO site (e.g. up-valley wind or vertical mixing) except  
454 during late winter and early spring (Fig. 6a, b). Concurrently, the WVMRs at the TRO site  
455 were consistently lower than the threshold of 5.25 g/kg during late winter and early spring,  
456 suggesting that the site is primarily influenced by free tropospheric (FT) air (Fig. 6b). The  
457 pattern was reinforced by the analysis of PBLH, exhibiting similar seasonal cycle. The  
458 monthly median PBLH was found to be lower than the altitude of the TRO site during late  
459 winter and early spring, and higher for the remainder of the year. We further calculated the  
460 occurrence frequency of PBLH at AMX exceeding the altitude of the TRO site (1287 m above  
461 AMX) and WVMR at TRO exceeding a threshold value of 5.25 g/kg. The occurrence  
462 frequencies demonstrate the observed seasonal and diurnal patterns in PBL influence on the  
463 TRO site (Figs. 6d, 6e). This suggests that the TRO site is periodically influenced by the PBL  
464 evolution during later winter and early spring, whereas it is primarily within the PBL for the  
465 remainder of the year. Lastly, Figure 6f shows the monthly fraction of days when the TRO site  
466 is influenced by the evolution of PBL. The TRO site is within the PBL on approximately 25%  
467 of days during late winter and early spring, increasing to >80% for the remainder of the year.  
468 The concurrent patterns observed in these tracers (PBLH and WVMR) suggest that the TRO  
469 site is impacted by the transport of polluted air from lower-elevation regions, possibly through

470 vertical mixing or up-valley wind. Previous studies have demonstrated that up-valley winds  
 471 can facilitate the upward movement of aerosol precursors, which can rapidly form a large  
 472 number of new aerosol particles, and pre-existing particles from lower-altitude regions to  
 473 mountain measurement sites, particularly within an elevated PBL (Bianchi et al., 2021; Hooda  
 474 et al., 2018; Sebastian et al., 2021; Cusack et al., 2013).



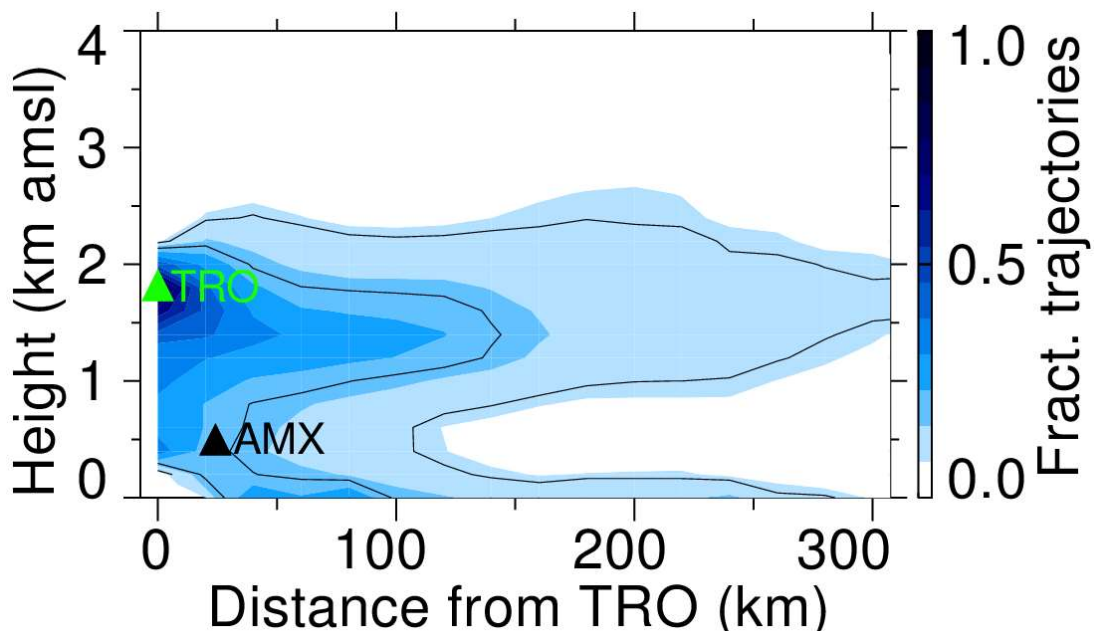
475

476 **Figure 6.** Monthly median diurnal variation of WVMR at (a) AMX, (b) TRO, and (c) PBLH  
 477 at AMX. The pixels with a plus sign in (c) indicate the times of the day when PBLH is higher  
 478 than the altitude of the TRO site (1287 m above the AMX site). (d) monthly median diurnal  
 479 variation of the occurrence frequency of PBLH higher than the altitude of the TRO site, (e)  
 480 monthly median diurnal variation of the occurrence frequency of WVMR > 5.25 g/kg at TRO,  
 481 indicative of the PBL evolution up to the altitude of the TRO site, and (f) monthly fraction of

482 days the TRO site is influenced by the evolution of PBL as illustrated by PBLH higher than  
483 the altitude of the TRO site and WVMR > 5.25 g/kg at TRO. The grey thin lines in (a)-(e)  
484 indicate UTC sunrise and sunset times.

485

486 To further substantiate our hypothesis, we examined the air mass history at the TRO site during  
487 observed concurrent NPF event days. Figure 7 shows the vertical cross-section of the fraction  
488 of air mass backward trajectories arriving at the TRO for observed concurrent NPF events. A  
489 large fraction of air masses had spent considerable time within the PBL before ascending to  
490 the altitude of the TRO site during concurrent NPF events at TRO. The monthly averaged  
491 air mass backward trajectories on concurrent NPF events showed that the free tropospheric air  
492 masses descended into the PBL upon entering the Mediterranean Sea, then they travelled along  
493 the surface towards the AMX site (Fig. S6) and eventually ascended to the TRO site altitude  
494 and above in response to the evolving PBL during the day (Fig. 7). The amplitude of the diurnal  
495 pattern of aerosol properties is the highest for the concurrent NPF events (Figs. 4, 5), further  
496 substantiating that the TRO site experiences daytime evolution of the PBL, analogous to a  
497 previous study demonstrating the daytime PBL influence due to vertical mixing (Collaud Coen  
498 et al., 2018). On the other hand, the air mass backward trajectories on individual NPF event  
499 days at these sites show distinct air mass history (Fig. S7).



500

501 **Figure 7.** Vertical cross-section of the fraction of air mass backward trajectories arriving at the  
502 TRO site (6 - 12 UTC) for the observed concurrent NPF events. The green and black upward  
503 triangle indicates TRO and AMX elevation above mean sea level, respectively.

504

#### 505 **4. Discussions**

506 The frequency of occurrence of NPF events was comparable between AMX (a lower-altitude  
507 rural site) and TRO (a higher-altitude mountain site) in Cyprus, as opposed to the findings of  
508 Boulon et al. (2011) in Central France, where NPF events were more frequent at a mountain  
509 site (the Puy de Dôme station, 1465 m a.m.s.l.) than at a nearby rural lower-altitude site (the  
510 Opme station, 660 m a.m.s.l., about 12 km southeast of the Puy de Dôme station). The follow-  
511 up study by Farah et al. (2018) used PBL tracers, such as particle size distribution and black  
512 carbon concentrations, to distinguish between free-tropospheric and PBL air masses at Puy de  
513 Dôme. They found that the Puy de Dôme station is within the PBL 50% of the time during the  
514 winter and up to 97% during the summer. **Since most mountain sites are typically within the  
515 PBL during the day, it is important to investigate whether the evolving PBL influences these  
516 mountain sites when NPF occurs.** The AMX and TRO sites are also located close to each other,  
517 approximately 20 km apart, yet we observed similar NPF frequencies at both (Fig. 3a). About  
518 half of the NPF events occurred simultaneously at both sites (Fig. 3d), particularly when the  
519 air masses originated from the northwest to northeast corridor relative to the TRO site. At  
520 measurement sites situated above 1000 m a.s.l., higher condensation sink tend to favour NPF,  
521 likely due to the presence of precursor gases needed to initiate nucleation and early growth  
522 (Sellegri et al., 2019), which is thought to be linked to vertically elevated precursor gases that  
523 promote particle formation and growth (in our case, SO<sub>2</sub> concentrations **were higher** during  
524 NPF events than non-events at TRO, **Fig. S3c**). Measurements from a remote background site  
525 in the western Himalayas also indicated that NPF was favoured under the influence of  
526 anthropogenic plumes with a higher condensation sink indicative of the precursor- and aerosol-  
527 laden air (Sebastian et al., 2021). Measurements from a **remote** mountain site (Mount Heng,  
528 Huan Province) in South China further demonstrated that NPF events are favoured during  
529 heavy dust episodes mixed with anthropogenic pollution (Nie et al., 2014). All of these studies  
530 suggest that the balance between precursor vapours and pre-existing particles in homogeneously  
531 mixed air masses determines when NPF is favoured in the atmosphere (Kanawade et al., 2021;  
532 Hyvärinen et al., 2010).

533

534 A previous study demonstrated that the 30-minute time lag between black carbon  
535 concentrations and the cluster ion mode suggests that nucleation processes may be initiated at  
536 the interface between the PBL and the free troposphere (Sellegrri et al., 2019). However, the 1–  
537 2 hour time lag and the higher magnitude of aerosol properties at the AMX site compared to  
538 TRO (Figs. 4, S2, S3c, and S4a) suggest nucleation processes likely occurred within the well-  
539 mixed PBL. Airborne observations of sub-3 nm particles over boreal forests showed that the  
540 total particle number concentrations ( $>1.5$  nm) are the highest near the ground in the morning,  
541 and the aerosol population is well mixed within evolving PBL later in the day (Leino et al.,  
542 2019). Crumeyrolle et al. (2010) also showed that nucleation occurs within the boundary layer,  
543 with the vertical extension of NPF events not exceeding the boundary layer's top. This can be  
544 explained by turbulent mixing leading to local supersaturation of condensable vapours and the  
545 dispersion of pre-existing particles, which in turn could enhance the nucleation process within  
546 the well-mixed PBL. Even at higher-altitude sites like the Jungfraujoch station (3580 m  
547 a.m.s.l.), previous studies have shown that NPF events can occur in free tropospheric air  
548 masses, provided these air masses are in contact with the PBL before reaching to higher-altitude  
549 site (Bianchi et al., 2016; Tröstl et al., 2016b). Carnerero et al. (2018) also showed that ultrafine  
550 particles are formed within the mixed layer, and as this layer expands, these particles are  
551 subsequently detected at higher altitudes within the PBL. On the contrary, Platis et al. (2016)  
552 provided observational evidence of the inversion layer facilitating thermodynamic conditions  
553 for NPF at elevated altitudes within the PBL, and subsequently, these particles moved toward  
554 the ground. Several other studies also showed that NPF events preferentially take place in the  
555 free troposphere (Clarke and Kapustin, 2002; Hamburger et al., 2011; Rose et al., 2015), or at  
556 the interface between the PBL and the free troposphere (Wehner et al., 2015).

557

558 Nonetheless, only about 50% of NPF events occurred concurrently at both sites when air  
559 masses originated from the northwest to northeast corridor (with AMX located north-northeast  
560 of TRO). Figure S7 illustrates the monthly-averaged, two-day backward air mass trajectories  
561 as a function of altitude for NPF events at AMX and TRO. Despite the proximity of these sites  
562 (~20 km), NPF events often occur in distinct air masses (Fig. S7). At TRO, the remaining  
563 events were linked to free-tropospheric air masses or the PBL under similar conditions, with  
564 air masses arriving from the southwest to the southeast corridor. Air mass history together with  
565 the intense solar radiation, the intricate mixture of both natural and anthropogenic emissions  
566 from continental and marine origins, the presence of local breeze systems (mountain, valley,  
567 sea, and land) and elevated dust layers over the region poses a significant challenge in

568 understanding the drivers behind the frequent NPF events observed in Cyprus and, therefore  
569 adds complexity to the PBL–NPF relationship.

570

## 571 **5. Conclusions**

572 This work presents the concurrent observations of ion and particle size distributions from a  
573 rural background lower-altitude site (Agia Marina Xyliatou, 532 m a.m.s.l.) and a higher-  
574 altitude background mountain site (Troodos, 1819 m a.m.s.l.) in Cyprus for the year 2022. We  
575 investigated the influence of boundary layer evolution on the NPF occurrence at a background  
576 mountain site, TRO. We found that the NPF event frequency was comparable between AMX  
577 (129 days out of 214 valid observation days, 60%) and TRO (121 days out of 224 valid  
578 observation days, 54%). Out of these, NPF events occurred concurrently at both sites on 69  
579 days. Typical NPF events at AMX and TRO exhibited distinct patterns, with AMX showing a  
580 significantly longer-lasting banana-shaped distribution below 10 nm diameter compared to  
581 TRO, suggesting differences in the supply of precursor vapours. During concurrent NPF  
582 events, the smaller mode diameter at the AMX site implies that nucleation processes occur  
583 nearby, while the particles have grown larger before they are detected at TRO.

584

585 By combining measurements from the higher-altitude TRO site with those from the lower-  
586 altitude AMX site, we were able to investigate the influence of evolving PBL on the nucleation  
587 processes in this remote mountainous region. For this, we used ceilometer measurements from  
588 AMX along with WVMR, passive tracers of PBL dynamics, from both sites to examine the  
589 diurnal evolution of the PBL. Our analyses indicated that the TRO site is within the PBL on  
590 approximately 25% of days during late winter and early spring, increasing to >80% of days for  
591 the remainder of the year. We used 69 days of concurrent NPF events days and compared them  
592 with individual NPF events at both sites. The peak in size-segregated ion and particle number  
593 concentrations occurred at the same time of day for individual NPF events at **both sites. In**  
594 **contrast, for** concurrent NPF events, the peak was observed at the lower-altitude site first,  
595 followed by a 1-2 hour time delay at the mountain site, TRO, suggesting the vertical extent of  
596 the nucleation process within the PBL. In these cases, NPF events at TRO are linked to the  
597 evolving PBL since the nucleation is detected at TRO when the PBL extends over the altitude  
598 of the TRO site. This was substantiated by a 1-hour delay in the NPF events start-time and a  
599 relatively larger particle mode diameter at TRO. This suggests that the transport of precursor  
600 vapour-laden air from lower-altitude regions, likely driven by vertical mixing or up-valley  
601 winds, might play a significant role in the aerosol formation process in the higher-altitude site.



602 The airmass history for concurrent NPF events revealed that a significant fraction of the  
603 airmass trajectories had previously been in contact with the PBL before reaching the TRO site.  
604 This suggests the vertical extent of NPF processes within the evolving PBL, though this  
605 requires further critical investigation. The influence of evolving PBL at a mountain site in this  
606 study reflects similarities with those reported in earlier studies, showing observed NPF events  
607 at a higher-altitude site, whether within or above PBL, have always been linked with the PBL  
608 (Bianchi et al., 2016; Carnerero et al., 2018; Sebastian et al., 2021; Sellegri et al., 2019; Bianchi  
609 et al., 2021; Hooda et al., 2018), except those observed in the middle-upper troposphere and  
610 stratosphere or convective cloud outflows.

611

612 **Despite significant progress in regional and global climate models enhanced with process-**  
613 **based parameterisations derived from controlled laboratory experiments, ambient**  
614 **measurements, and space-borne observations, a comprehensive understanding of the climate**  
615 **system remains elusive. The aerosol-cloud interaction is one of the largest sources of**  
616 **uncertainty in the climate system, primarily due to ambiguity in CCN production, which arises**  
617 **from uncertainties in both primary emissions and airborne secondary production (IPCC, 2023).**  
618 **Furthermore, the uneven geographical distribution and spatial heterogeneity of measurement**  
619 **networks, coupled with asynchronous monitoring and inconsistent data collection methods for**  
620 **various atmospheric variables hinder the ability to constrain model assimilation and validation.**  
621 **Thus, the process-level understanding of atmospheric processes, their interactions and**  
622 **feedback from them, such as the intricate mixture of primary emissions and airborne production**  
623 **of aerosols, is crucial for advancing future climate predictions, particularly the EMME region**  
624 **which has been recognised as a global climate change hotspot with high vulnerability to climate**  
625 **change impacts.**

626

#### 627 ***Data availability.***

628 In-situ measurements of ion and particle size distributions, meteorological parameters and  
629 gases can be accessed at Zenodo (DOI: <https://doi.org/10.5281/zenodo.13970203>). The  
630 ceilometer data can be viewed at <https://e-profile.eu/> (last accessed 22 October 2024). ERA5  
631 boundary layer height data is publicly available from  
632 <https://cds.climate.copernicus.eu/datasets/reanalysis-era5-single-levels> (last accessed 22  
633 October 2024). AERONET aerosol optical depth and Ångström exponent data are available  
634 publicly to download from <https://aeronet.gsfc.nasa.gov/> (last accessed 22 October 2024)

635

636 ***Author contributions***

637 FM, JS, MK, KL and TJ designed the experiments and ND, AP, RB, and MP carried them out.  
638 ND, VPK and AP analysed the data. ND, VPK and TJ prepared the manuscript with  
639 contributions from all co-authors.

640

641 ***Competing interests.***

642 At least one of the (co-)authors is a member of the editorial board of Aerosol Research. The  
643 authors declare that they have no conflict of interest.

644

645 ***Acknowledgements.***

646 This work has been supported by the European Union's Horizon 2020 Research and Innovation  
647 Programme under grant agreement No. 856612 and the Cyprus Government. TJ acknowledges  
648 the funding support by the European Union ERC-2022-STGERC-BAE-Project: 101076311.  
649 Views and opinions expressed are however those of the author(s) only and do not necessarily  
650 reflect those of the European Union or the European Research Council Executive Agency.  
651 Neither the European Union nor the granting authority can be held responsible for them. The  
652 authors thank the University of Helsinki, INAR/Physics for support and instrumentation. The  
653 authors also thank the technical support team; Nikoleta Lekaki, Moreno Parolin, and Rafail  
654 Konatzii for the technical support in maintaining field stations. The authors thank all the past  
655 and present personnel who contributed to the field measurements within the EMME project.

656 **The authors thank the anonymous reviewers for their valuable suggestions and comments.**

657

658 **References**

659 Aktypis, A., Kaltsonoudis, C., Skyllakou, K., Matrali, A., Vasilakopoulou, C. N., Florou, K.,  
660 and Pandis, S. N.: Infrequent new particle formation in a coastal Mediterranean city during the  
661 summer, *Atmos. Environ.*, 302, 119732, <https://doi.org/10.1016/j.atmosenv.2023.119732>,  
662 2023.

663 Aktypis, A., Kaltsonoudis, C., Patoulias, D., Kalkavouras, P., Matrali, A., Vasilakopoulou, C.  
664 N., Kostenidou, E., Florou, K., Kalivitis, N., Bougiatioti, A., Eleftheriadis, K., Vratolis, S.,  
665 Gini, M. I., Kouras, A., Samara, C., Lazaridis, M., Chatoutsidou, S. E., Mihalopoulos, N., and  
666 Pandis, S. N.: Significant spatial gradients in new particle formation frequency in Greece  
667 during summer, *Atmos. Chem. Phys.*, 24, 65-84, <https://doi.org/10.5194/acp-24-65-2024>,  
668 2024.

669 Baalbaki, R., Pikridas, M., Jokinen, T., Laurila, T., Dada, L., Bezantakos, S., Ahonen, L.,  
670 Neitola, K., Maisser, A., Bimenyimana, E., Christodoulou, A., Unga, F., Savvides, C.,  
671 Lehtipalo, K., Kangasluoma, J., Biskos, G., Petäjä, T., Kerminen, V. M., Sciare, J., and

672 Kulmala, M.: Towards understanding the characteristics of new particle formation in the  
673 Eastern Mediterranean, *Atmos. Chem. Phys.*, 21, 9223-9251, [https://doi.org/10.5194/acp-21-](https://doi.org/10.5194/acp-21-9223-2021)  
674 9223-2021, 2021.

675 Bianchi, F., Junninen, H., Bigi, A., Sinclair, V. A., Dada, L., Hoyle, C. R., Zha, Q., Yao, L.,  
676 Ahonen, L. R., Bonasoni, P., Buenrostro Mazon, S., Hutterli, M., Laj, P., Lehtipalo, K.,  
677 Kangasluoma, J., Kerminen, V. M., Kontkanen, J., Marinoni, A., Mirme, S., Molteni, U.,  
678 Petäjä, T., Riva, M., Rose, C., Sellegri, K., Yan, C., Worsnop, D. R., Kulmala, M.,  
679 Baltensperger, U., and Dommen, J.: Biogenic particles formed in the Himalaya as an important  
680 source of free tropospheric aerosols, *Nat. Geosci.*, 14, 4-9, [https://doi.org/10.1038/s41561-020-](https://doi.org/10.1038/s41561-020-00661-5)  
681 00661-5, 2021.

682 Bianchi, F., Tröstl, J., Junninen, H., Frege, C., Henne, S., Hoyle, C. R., Molteni, U., Herrmann,  
683 E., Adamov, A., Bukowiecki, N., Chen, X., Duplissy, J., Gysel, M., Hutterli, M., Kangasluoma,  
684 J., Kontkanen, J., Kürten, A., Manninen, H. E., Münch, S., Peräkylä, O., Petäjä, T., Rondo, L.,  
685 Williamson, C., Weingartner, E., Curtius, J., Worsnop, D. R., Kulmala, M., Dommen, J., and  
686 Baltensperger, U.: New particle formation in the free troposphere: A question of chemistry and  
687 timing, *Science*, 352, 1109-1112, <https://doi.org/10.1126/science.aad5456>, 2016.

688 Bimenyimana, E., Pikridas, M., Oikonomou, K., Iakovides, M., Christodoulou, A., Sciare, J.,  
689 and Mihalopoulos, N.: Fine aerosol sources at an urban background site in the Eastern  
690 Mediterranean (Nicosia; Cyprus): Insights from offline versus online source apportionment  
691 comparison for carbonaceous aerosols, *Sci. Total Environ.*, 893, 164741,  
692 <https://doi.org/10.1016/j.scitotenv.2023.164741>, 2023.

693 Boulon, J., Sellegri, K., Hervo, M., Picard, D., Pichon, J. M., Fréville, P., and Laj, P.:  
694 Investigation of nucleation events vertical extent: a long term study at two different altitude  
695 sites, *Atmos. Chem. Phys.*, 11, 5625-5639, <https://doi.org/10.5194/acp-11-5625-2011>, 2011.

696 Brilke, S., Fölker, N., Müller, T., Kandler, K., Gong, X., Peischl, J., Weinzierl, B., and Winkler,  
697 P. M.: New particle formation and sub-10 nm size distribution measurements during the A-  
698 LIFE field experiment in Paphos, Cyprus, *Atmos. Chem. Phys.*, 20, 5645-5656,  
699 <https://doi.org/10.5194/acp-20-5645-2020>, 2020.

700 Buck, A. L.: New Equations for Computing Vapor Pressure and Enhancement Factor, *J. Appl.*  
701 *Meteorol. Climatol.*, 20, 1527-1532, [https://doi.org/10.1175/1520-](https://doi.org/10.1175/1520-0450(1981)020<1527:NEFCVP>2.0.CO;2)  
702 0450(1981)020<1527:NEFCVP>2.0.CO;2, 1981.

703 Buenrostro Mazon, S., Riipinen, I., Schultz, D. M., Valtanen, M., Dal Maso, M., Sogacheva,  
704 L., Junninen, H., Nieminen, T., Kerminen, V.-M., and Kulmala, M.: Classifying previously  
705 undefined days from eleven years of aerosol-particle-size distribution data from the SMEAR  
706 II station, Hyytiälä, Finland, *Atmos. Chem. Phys.*, 9, 667-676, [https://doi.org/10.5194/acp-9-](https://doi.org/10.5194/acp-9-667-2009)  
707 667-2009, 2009.

708 Carnerero, C., Pérez, N., Reche, C., Ealo, M., Titos, G., Lee, H. K., Eun, H. R., Park, Y. H.,  
709 Dada, L., Paasonen, P., Kerminen, V. M., Mantilla, E., Escudero, M., Gómez-Moreno, F. J.,  
710 Alonso-Blanco, E., Coz, E., Saiz-Lopez, A., Temime-Roussel, B., Marchand, N., Beddows, D.  
711 C. S., Harrison, R. M., Petäjä, T., Kulmala, M., Ahn, K. H., Alastuey, A., and Querol, X.:  
712 Vertical and horizontal distribution of regional new particle formation events in Madrid,  
713 *Atmos. Chem. Phys.*, 18, 16601-16618, <https://doi.org/10.5194/acp-18-16601-2018>, 2018.

714 Clarke, A. D. and Kapustin, V. N.: A Pacific Aerosol Survey. Part I: A Decade of Data on  
715 Particle Production, Transport, Evolution, and Mixing in the Troposphere *J. Atmos. Sci.*, 59,  
716 363-382, [https://doi.org/10.1175/1520-0469\(2002\)059<0363:APASPI>2.0.CO;2](https://doi.org/10.1175/1520-0469(2002)059<0363:APASPI>2.0.CO;2), 2002.

717 Clarke, A. D., Varner, J. L., Eisele, F., Mauldin, R. L., Tanner, D., and Litchy, M.: Particle  
718 production in the remote marine atmosphere: Cloud outflow and subsidence during ACE 1, *J.*  
719 *Geophys. Res.*103, 16397-16409, <https://doi.org/10.1029/97JD02987>, 1998.

720 Collaud Coen, M., Andrews, E., Aliaga, D., Andrade, M., Angelov, H., Bukowiecki, N., Ealo,  
721 M., Fialho, P., Flentje, H., Hallar, A. G., Hooda, R., Kalapov, I., Krejci, R., Lin, N. H.,  
722 Marinoni, A., Ming, J., Nguyen, N. A., Pandolfi, M., Pont, V., Ries, L., Rodríguez, S., Schauer,  
723 G., Sellegri, K., Sharma, S., Sun, J., Tunved, P., Velasquez, P., and Ruffieux, D.: Identification  
724 of topographic features influencing aerosol observations at high altitude stations, *Atmos.*  
725 *Chem. Phys.*, 18, 12289-12313, <https://doi.org/10.5194/acp-18-12289-2018>, 2018.

726 Crumeyrolle, S., Manninen, H. E., Sellegri, K., Roberts, G., Gomes, L., Kulmala, M., Weigel,  
727 R., Laj, P., and Schwarzenboeck, A.: New particle formation events measured on board the  
728 ATR-42 aircraft during the EUCAARI campaign, *Atmos. Chem. Phys.*, 10, 6721-6735,  
729 <https://doi.org/10.5194/acp-10-6721-2010>, 2010.

730 Cusack, M., Alastuey, A., and Querol, X.: Case studies of new particle formation and  
731 evaporation processes in the western Mediterranean regional background, *Atmos. Environ.*, 81,  
732 651-659, <https://doi.org/10.1016/j.atmosenv.2013.09.025>, 2013.

733 Dal Maso, M., Kulmala, M., Riipinen, I., Wagner, R., Hussein, T., Aalto, P. P., and Lehtinen,  
734 K. E. J.: Formation and growth of fresh atmospheric aerosols: eight years of aerosol size  
735 distribution data from SMEAR II, Hyytiälä, Finland, *Boreal Env. Res.*, 10, 323-336, ISSN  
736 1239-6095, 2005.

737 Debevec, C., Sauvage, S., Gros, V., Sellegri, K., Sciare, J., Pikridas, M., Stavroulas, I.,  
738 Leonardis, T., Gaudion, V., Depelchin, L., Fronval, I., Sarda-Estève, R., Baisnée, D., Bonsang,  
739 B., Savvides, C., Vrekoussis, M., and Locoge, N.: Driving parameters of biogenic volatile  
740 organic compounds and consequences on new particle formation observed at an eastern  
741 Mediterranean background site, *Atmos. Chem. Phys.*, 18, 14297-14325,  
742 <https://doi.org/10.5194/acp-18-14297-2018>, 2018.

743 Dinoi, A., Gulli, D., Weinhold, K., Ammoscato, I., Calidonna, C. R., Wiedensohler, A., and  
744 Contini, D.: Characterization of ultrafine particles and the occurrence of new particle formation  
745 events in an urban and coastal site of the Mediterranean area, *Atmos. Chem. Phys.*, 23, 2167-  
746 2181, <https://doi.org/10.5194/acp-23-2167-2023>, 2023.

747 Draxler, R. R. and Rolph, G. D.: HYSPLIT (HYbrid Single-Particle Lagrangian Integrated  
748 Trajectory) Model Access via NOAA ARL READY Website. NOAA Air Resources  
749 Laboratory, Silver Spring. <http://ready.arl.noaa.gov/HYSPLIT.php>, 2010.

750 Emeis, S., Jahn, C., Münkler, C., Münsterer, C., and Schäfer, K.: Multiple atmospheric layering  
751 and mixing-layer height in the Inn valley observed by remote sensing, *Meteorol. Z.*, 16, 415-  
752 424, <https://doi.org/10.1127/0941?2948/2007/0203>, 2007.

753 Farah, A., Freney, E., Chauvigné, A., Baray, J.-L., Rose, C., Picard, D., Colomb, A., Hadad,  
754 D., Abboud, M., Farah, W., and Sellegri, K.: Seasonal variation of aerosol size distribution data

755 at the Puy de Dôme station with emphasis on the boundary layer/free troposphere segregation,  
756 *Atmosphere*, 9, 244, <https://doi.org/10.3390/atmos9070244>, 2018.

757 Gong, X., Wex, H., Müller, T., Wiedensohler, A., Höhler, K., Kandler, K., Ma, N., Dietel, B.,  
758 Schiebel, T., Möhler, O., and Stratmann, F.: Characterization of aerosol properties at Cyprus,  
759 focusing on cloud condensation nuclei and ice-nucleating particles, *Atmos. Chem. Phys.*, 19,  
760 10883-10900, 10.5194/acp-19-10883-2019, 2019.

761 Gordon, H., Kirkby, J., Baltensperger, U., Bianchi, F., Breitenlechner, M., Curtius, J., Dias, A.,  
762 Dommen, J., Donahue, N. M., Dunne, E. M., Duplissy, J., Ehrhart, S., Flagan, R. C., Frege, C.,  
763 Fuchs, C., Hansel, A., Hoyle, C. R., Kulmala, M., Kürten, A., Lehtipalo, K., Makhmutov, V.,  
764 Molteni, U., Rissanen, M. P., Stozkhov, Y., Tröstl, J., Tsagkogeorgas, G., Wagner, R.,  
765 Williamson, C., Wimmer, D., Winkler, P. M., Yan, C., and Carslaw, K. S.: Causes and  
766 importance of new particle formation in the present-day and preindustrial atmospheres, *J.*  
767 *Geophys. Res.*, 122, 8739-8760, <https://doi.org/10.1002/2017jd026844>, 2017.

768 Gormley, P. G. and Kennedy, M.: Diffusion from a Stream Flowing Through a Cylindrical  
769 Tube, *Proc. R. Ir. Acad., Sect. A*, 52, 163-169, <https://www.jstor.org/stable/20488498>, 1949.

770 Hakala, S., Vakkari, V., Lihavainen, H., Hyvärinen, A. P., Neitola, K., Kontkanen, J.,  
771 Kerminen, V. M., Kulmala, M., Petäjä, T., Hussein, T., Khoder, M. I., Alghamdi, M. A., and  
772 Paasonen, P.: Explaining apparent particle shrinkage related to new particle formation events  
773 in western Saudi Arabia does not require evaporation, *Atmos. Chem. Phys.*, 23, 9287-9321,  
774 <https://doi.org/10.5194/acp-23-9287-2023>, 2023.

775 Hakala, S., Alghamdi, M. A., Paasonen, P., Vakkari, V., Khoder, M. I., Neitola, K., Dada, L.,  
776 Abdelmaksoud, A. S., Al-Jeelani, H., Shabbaj, I. I., Almeahmadi, F. M., Sundström, A. M.,  
777 Lihavainen, H., Kerminen, V. M., Kontkanen, J., Kulmala, M., Hussein, T., and Hyvärinen, A.  
778 P.: New particle formation, growth and apparent shrinkage at a rural background site in western  
779 Saudi Arabia, *Atmos. Chem. Phys.*, 19, 10537-10555, [https://doi.org/10.5194/acp-19-10537-](https://doi.org/10.5194/acp-19-10537-2019)  
780 2019, 2019.

781 Hamburger, T., McMeeking, G., Minikin, A., Birmili, W., Dall'Osto, M., O'Dowd, C., Flentje,  
782 H., Henzing, B., Junninen, H., Kristensson, A., de Leeuw, G., Stohl, A., Burkhart, J. F., Coe,  
783 H., Krejci, R., and Petzold, A.: Overview of the synoptic and pollution situation over Europe  
784 during the EUCAARI-LONGREX field campaign, *Atmos. Chem. Phys.*, 11, 1065-1082,  
785 <https://doi.org/10.5194/acp-11-1065-2011>, 2011.

786 Hersbach, H., Bell, B., Berrisford, P., Biavati, G., Horányi, A., Muñoz Sabater, J., Nicolas, J.,  
787 Peubey, C., Radu, R., Rozum, I., Schepers, D., Simmons, A., Soci, C., Dee, D., and Thépaut,  
788 J.-N.: ERA5 hourly data on pressure levels from 1940 to present. Copernicus Climate Change  
789 Service (C3S) Climate Data Store (CDS), <https://doi.org/10.24381/cds.bd0915c6>, 2023.

790 Hersbach, H., Bell, B., Berrisford, P., Hirahara, S., Horányi, A., Muñoz-Sabater, J., Nicolas,  
791 J., Peubey, C., Radu, R., Schepers, D., Simmons, A., Soci, C., Abdalla, S., Abellan, X.,  
792 Balsamo, G., Bechtold, P., Biavati, G., Bidlot, J., Bonavita, M., De Chiara, G., Dahlgren, P.,  
793 Dee, D., Diamantakis, M., Dragani, R., Flemming, J., Forbes, R., Fuentes, M., Geer, A.,  
794 Haimberger, L., Healy, S., Hogan, R. J., Hólm, E., Janisková, M., Keeley, S., Laloyaux, P.,  
795 Lopez, P., Lupu, C., Radnoti, G., de Rosnay, P., Rozum, I., Vamborg, F., Villaume, S., and  
796 Thépaut, J.-N.: The ERA5 global reanalysis, *Q. J. R. Meteorol. Soc.*, 146, 1999-2049,  
797 <https://doi.org/10.1002/qj.3803>, 2020.

798 Hirsikko, A., Bergman, T., Laakso, L., Dal Maso, M., Riipinen, I., Hörrak, U., and Kulmala,  
799 M.: Identification and classification of the formation of intermediate ions measured in boreal  
800 forest, *Atmos. Chem. Phys.*, 7, 201-210, <https://doi.org/10.5194/acp-7-201-2007>, 2007.

801 Hirsikko, A., Vakkari, V., Tiitta, P., Manninen, H. E., Gagné, S., Laakso, H., Kulmala, M.,  
802 Mirme, A., Mirme, S., Mabaso, D., Beukes, J. P., and Laakso, L.: Characterisation of sub-  
803 micron particle number concentrations and formation events in the western Bushveld Igneous  
804 Complex, South Africa, *Atmos. Chem. Phys.*, 12, 3951-3967, <https://doi.org/10.5194/acp-12-3951-2012>, 2012.

806 Hooda, R. K., Kivekäs, N., O'Connor, E. J., Collaud Coen, M., Pietikäinen, J.-P., Vakkari, V.,  
807 Backman, J., Henriksson, S. V., Asmi, E., Komppula, M., Korhonen, H., Hyvärinen, A.-P., and  
808 Lihavainen, H.: Driving Factors of Aerosol Properties Over the Foothills of Central Himalayas  
809 Based on 8.5 Years Continuous Measurements, *J. Geophys. Res.*, 123, 13,421-413,442,  
810 <https://doi.org/10.1029/2018jd029744>, 2018.

811 Hussein, T., Atashi, N., Sogacheva, L., Hakala, S., Dada, L., Petäjä, T., and Kulmala, M.:  
812 Characterization of Urban New Particle Formation in Amman—Jordan, *Atmosphere*, 11, 79,  
813 <https://doi.org/10.3390/atmos11010079> 2020.

814 Hyvärinen, A. P., Lihavainen, H., Komppula, M., Panwar, T. S., Sharma, V. P., Hooda, R. K.,  
815 and Viisanen, Y.: Aerosol measurements at the Gual Pahari EUCAARI station: preliminary  
816 results from in-situ measurements, *Atmos. Chem. Phys.*, 10, 7241-7252,  
817 <https://doi.org/10.5194/acp-10-7241-2010>, 2010.

818 IPCC: Climate Change 2023: Synthesis Report. Contribution of Working Groups I, II and III  
819 to the Sixth Assessment Report of the Intergovernmental Panel on Climate Change [Core  
820 Writing Team, H. Lee and J. Romero (eds.)]. IPCC, Geneva, Switzerland, 184 pp.,  
821 <http://doi.org/10.59327/IPCC/AR6-9789291691647>, 2023.

822 Kalivitis, N., Kerminen, V. M., Kouvarakis, G., Stavroulas, I., Tzitzikalaki, E., Kalkavouras,  
823 P., Daskalakis, N., Myriokefalitakis, S., Bougiatioti, A., Manninen, H. E., Roldin, P., Petäjä,  
824 T., Boy, M., Kulmala, M., Kanakidou, M., and Mihalopoulos, N.: Formation and growth of  
825 atmospheric nanoparticles in the eastern Mediterranean: results from long-term measurements  
826 and process simulations, *Atmos. Chem. Phys.*, 19, 2671-2686, <https://doi.org/10.5194/acp-19-2671-2019>, 2019.

828 Kalkavouras, P., Bougiatioti, A., Hussein, T., Kalivitis, N., Stavroulas, I., Michalopoulos, P.,  
829 and Mihalopoulos, N.: Regional New Particle Formation over the Eastern Mediterranean and  
830 Middle East, *Atmosphere*, 12, <https://doi.org/10.3390/atmos12010013>, 2021.

831 Kalkavouras, P., Bougiatioti, A., Kalivitis, N., Stavroulas, I., Tombrou, M., Nenes, A., and  
832 Mihalopoulos, N.: Regional new particle formation as modulators of cloud condensation nuclei  
833 and cloud droplet number in the eastern Mediterranean, *Atmos. Chem. Phys.*, 19, 6185-6203,  
834 <https://doi.org/10.5194/acp-19-6185-2019>, 2019.

835 Kalkavouras, P., Bougiatioti, A., Grivas, G., Stavroulas, I., Kalivitis, N., Liakakou, E.,  
836 Gerasopoulos, E., Pilinis, C., and Mihalopoulos, N.: On the regional aspects of new particle  
837 formation in the Eastern Mediterranean: A comparative study between a background and an  
838 urban site based on long term observations, *Atmos. Res.*, 239, 104911,  
839 <https://doi.org/10.1016/j.atmosres.2020.104911>, 2020.

- 840 Kanawade, V. P., Sebastian, M., Hooda, R. K., and Hyvärinen, A. P.: Atmospheric new particle  
841 formation in India: Current understanding, knowledge gaps and future directions, *Atmos.*  
842 *Environ.*, 270, 118894, <https://doi.org/10.1016/j.atmosenv.2021.118894>, 2021.
- 843 Kanawade, V. P., Tripathi, S. N., Siingh, D., Gautam, A. S., Srivastava, A. K., Kamra, A. K.,  
844 Soni, V. K., and Sethi, V.: Observations of new particle formation at two distinct Indian  
845 subcontinental urban locations, *Atmos. Environ.*, 96, 370-379,  
846 <http://dx.doi.org/10.1016/j.atmosenv.2014.08.001>, 2014.
- 847 Kerminen, V. M., Chen, X., Vakkari, V., Petäjä, T., Kulmala, M., and Bianchi, F.: Atmospheric  
848 new particle formation and growth: review of field observations, *Environ. Res. Lett.*, 13,  
849 103003, <https://doi.org/10.1088/1748-9326/aadf3c>, 2018.
- 850 Kerminen, V. M., Paramonov, M., Anttila, T., Riipinen, I., Fountoukis, C., Korhonen, H.,  
851 Asmi, E., Laakso, L., Lihavainen, H., Swietlicki, E., Svenningsson, B., Asmi, A., Pandis, S.  
852 N., Kulmala, M., and Petäjä, T.: Cloud condensation nuclei production associated with  
853 atmospheric nucleation: a synthesis based on existing literature and new results, *Atmos. Chem.*  
854 *Phys.*, 12, 12037-12059, <https://doi.org/10.5194/acp-12-12037-2012>, 2012.
- 855 Kotthaus, S., Bravo-Aranda, J. A., Collaud Coen, M., Guerrero-Rascado, J. L., Costa, M. J.,  
856 Cimini, D., O'Connor, E. J., Hervo, M., Alados-Arboledas, L., Jiménez-Portaz, M., Mona, L.,  
857 Ruffieux, D., Illingworth, A., and Haefelin, M.: Atmospheric boundary layer height from  
858 ground-based remote sensing: a review of capabilities and limitations, *Atmos. Meas. Tech.*, 16,  
859 433-479, <https://doi.org/10.5194/amt-16-433-2023>, 2023.
- 860 Kulmala, M.: How Particles Nucleate and Grow, 302, 1000-1001,  
861 <https://doi.org/10.1126/science.1090848>, 2003.
- 862 Kulmala, M., Vehkamäki, H., Petäjä, T., Dal Maso, M., Lauri, A., Kerminen, V. M., Birmili,  
863 W., and McMurry, P. H.: Formation and growth rates of ultrafine atmospheric particles: a  
864 review of observations, *J. Aerosol Sci.*, 35, 143-176,  
865 <http://dx.doi.org/10.1016/j.jaerosci.2003.10.003>, 2004.
- 866 Kulmala, M., Aliaga, D., Tuovinen, S., Cai, R., Junninen, H., Yan, C., Bianchi, F., Cheng, Y.,  
867 Ding, A., Worsnop, D. R., Petäjä, T., Lehtipalo, K., Paasonen, P., and Kerminen, V. M.:  
868 Opinion: A paradigm shift in investigating the general characteristics of atmospheric new  
869 particle formation using field observations, *Aerosol Research*, 2, 49-58,  
870 <https://doi.org/10.5194/ar-2-49-2024>, 2024.
- 871 Kulmala, M., Petäjä, T., Nieminen, T., Sipilä, M., Manninen, H. E., Lehtipalo, K., Dal Maso,  
872 M., Aalto, P. P., Junninen, H., Paasonen, P., Riipinen, I., Lehtinen, K. E. J., Laaksonen, A., and  
873 Kerminen, V. M.: Measurement of the nucleation of atmospheric aerosol particles, *Nat. Protoc.*,  
874 7, 1651-1667, <https://doi.org/10.1038/nprot.2012.091>, 2012.
- 875 Lee, S.-H., Gordon, H., Yu, H., Lehtipalo, K., Haley, R., Li, Y., and Zhang, R.: New Particle  
876 Formation in the Atmosphere: From Molecular Clusters to Global Climate, *J. Geophys. Res.:*  
877 *Atmos.*, 124, 7098-7146, <https://doi.org/10.1029/2018JD029356>, 2019.
- 878 Leino, K., Lampilahti, J., Poutanen, P., Väänänen, R., Manninen, A., Buenrostro Mazon, S.,  
879 Dada, L., Franck, A., Wimmer, D., Aalto, P. P., Ahonen, L. R., Enroth, J., Kangasluoma, J.,  
880 Keronen, P., Korhonen, F., Laakso, H., Matilainen, T., Siivola, E., Manninen, H. E., Lehtipalo,

881 K., Kerminen, V. M., Petäjä, T., and Kulmala, M.: Vertical profiles of sub-3 nm particles over  
882 the boreal forest, *Atmos. Chem. Phys.*, 19, 4127-4138, 10.5194/acp-19-4127-2019, 2019.  
883

884 Lelieveld, J., Klingmüller, K., Pozzer, A., Burnett, R. T., Haines, A., and Ramanathan, V.:  
885 Effects of fossil fuel and total anthropogenic emission removal on public health and climate,  
886 *Proc. Natl. Acad. Sci.* 116, 7192-7197, <https://doi.org/10.1073/pnas.1819989116>, 2019.

887 Mäkelä, J. M., Riihelä, M., Ukkonen, A., Jokinen, V., and Keskinen, J.: Comparison of  
888 mobility equivalent diameter with Kelvin-Thomson diameter using ion mobility data, *J. Chem.*  
889 *Phys.*, 105, 1562-1571, <https://doi.org/10.1063/1.472017>, 1996.

890 Manninen, H. E., Mirme, S., Mirme, A., Petäjä, T., and Kulmala, M.: How to reliably detect  
891 molecular clusters and nucleation mode particles with Neutral cluster and Air Ion Spectrometer  
892 (NAIS), *Atmos. Meas. Tech.*, 9, 3577-3605, <https://doi.org/10.5194/amt-9-3577-2016>, 2016.

893 Manninen, H. E., Nieminen, T., Asmi, E., Gagné, S., Häkkinen, S., Lehtipalo, K., Aalto, P.,  
894 Vana, M., Mirme, A., Mirme, S., Hörrak, U., Plass-Dülmer, C., Stange, G., Kiss, G., Hoffer,  
895 A., Törő, N., Moerman, M., Henzing, B., de Leeuw, G., Brinkenberg, M., Kouvarakis, G. N.,  
896 Bougiatioti, A., Mihalopoulos, N., O'Dowd, C., Ceburnis, D., Arneth, A., Svenningsson, B.,  
897 Swietlicki, E., Tarozzi, L., Decesari, S., Facchini, M. C., Birmili, W., Sonntag, A.,  
898 Wiedensohler, A., Boulon, J., Sellegri, K., Laj, P., Gysel, M., Bukowiecki, N., Weingartner,  
899 E., Wehrle, G., Laaksonen, A., Hamed, A., Joutsensaari, J., Petäjä, T., Kerminen, V.-M., and  
900 Kulmala, M.: EUCAARI ion spectrometer measurements at 12 European sites – analysis of  
901 new particle formation events, *Atmos. Chem. Phys.*, 10, 7907-7927,  
902 <https://doi.org/10.5194/acp-10-7907-2010>, 2010.

903 Merikanto, J., Spracklen, D. V., Mann, G. W., Pickering, S. J., and Carslaw, K. S.: Impact of  
904 nucleation on global CCN, *Atmos. Chem. Phys.*, 9, 8601-8616, <https://doi.org/10.5194/acp-9-8601-2009>, 2009.

906 Minguillón, M. C., Brines, M., Pérez, N., Reche, C., Pandolfi, M., Fonseca, A. S., Amato, F.,  
907 Alastuey, A., Lyasota, A., Codina, B., Lee, H. K., Eun, H. R., Ahn, K. H., and Querol, X.: New  
908 particle formation at ground level and in the vertical column over the Barcelona area,  
909 *Atmospheric Research*, 164-165, 118-130, <https://doi.org/10.1016/j.atmosres.2015.05.003>,  
910 2015.

911 Mirme, S. and Mirme, A.: The mathematical principles and design of the NAIS – a  
912 spectrometer for the measurement of cluster ion and nanometer aerosol size distributions,  
913 *Atmos. Meas. Tech.*, 6, 1061-1071, <https://doi.org/10.5194/amt-6-1061-2013>, 2013.

914 Münkel, C. and Roininen, R.: Automatic monitoring of boundary layer structures with  
915 ceilometers, *Bound.-Lay. Meteorol.*, 124, 117-128, <https://doi.org/10.1007/s10546-006-9103-3>, 2010.

917 Nie, W., Ding, A., Wang, T., Kerminen, V.-M., George, C., Xue, L., Wang, W., Zhang, Q.,  
918 Petäjä, T., Qi, X., Gao, X., Wang, X., Yang, X., Fu, C., and Kulmala, M.: Polluted dust  
919 promotes new particle formation and growth, *Scientific Reports*, 4, 6634,  
920 <https://doi.org/10.1038/srep06634>, 2014.



- 921 Nieminen, T., Asmi, A., Maso, M. D., Aalto, P. P., Keronen, P., Petaja, T., Kulmala, M., and  
922 Kerminen, V.-M.: Trends in atmospheric new-particle formation: 16 years of observations in a  
923 boreal-forest environment, *Boreal Environ. Res.*, 19, 191-214, ISSN 1797-2469, 2014.
- 924 Nieminen, T., Kerminen, V. M., Petäjä, T., Aalto, P. P., Arshinov, M., Asmi, E., Baltensperger,  
925 U., Beddows, D. C. S., Beukes, J. P., Collins, D., Ding, A., Harrison, R. M., Henzing, B.,  
926 Hooda, R., Hu, M., Hörrak, U., Kivekäs, N., Komsaare, K., Krejci, R., Kristensson, A., Laakso,  
927 L., Laaksonen, A., Leaitch, W. R., Lihavainen, H., Mihalopoulos, N., Németh, Z., Nie, W.,  
928 O'Dowd, C., Salma, I., Sellegri, K., Svenningsson, B., Swietlicki, E., Tunved, P., Ulevicius,  
929 V., Vakkari, V., Vana, M., Wiedensohler, A., Wu, Z., Virtanen, A., and Kulmala, M.: Global  
930 analysis of continental boundary layer new particle formation based on long-term  
931 measurements, *Atmos. Chem. Phys.*, 18, 14737-14756, [https://doi.org/10.5194/acp-18-14737-](https://doi.org/10.5194/acp-18-14737-2018)  
932 2018, 2018.
- 933 O'Donnell, S. E., Akherati, A., He, Y., Hodshire, A. L., Shilling, J. E., Kuang, C., Fast, J. D.,  
934 Mei, F., Schobesberger, S., Thornton, J. A., Smith, J. N., Jathar, S. H., and Pierce, J. R.: Look  
935 Up: Probing the Vertical Profile of New Particle Formation and Growth in the Planetary  
936 Boundary Layer With Models and Observations, *J. Geophys. Res.*, 128, e2022JD037525,  
937 <https://doi.org/10.1029/2022JD037525>, 2023.
- 938 Pierce, J. R. and Adams, P. J.: Uncertainty in global CCN concentrations from uncertain  
939 aerosol nucleation and primary emission rates, *Atmos. Chem. Phys.*, 9, 1339-1356,  
940 <https://doi.org/10.5194/acp-9-1339-2009>, 2009.
- 941 Pikridas, M., Riipinen, I., Hildebrandt, L., Kostenidou, E., Manninen, H., Mihalopoulos, N.,  
942 Kalivitis, N., Burkhardt, J. F., Stohl, A., Kulmala, M., and Pandis, S. N.: New particle formation  
943 at a remote site in the eastern Mediterranean, *J. Geophys. Res.*, 117,  
944 <https://doi.org/10.1029/2012JD017570>, 2012.
- 945 Platis, A., Altstädter, B., Wehner, B., Wildmann, N., Lampert, A., Hermann, M., Birmili, W.,  
946 and Bange, J.: An Observational Case Study on the Influence of Atmospheric Boundary-Layer  
947 Dynamics on New Particle Formation, *Boundary-Layer Meteorology*, 158, 67-92,  
948 <https://doi.org/10.1007/s10546-015-0084-y>, 2016.
- 949 Rose, C., Sellegri, K., Freney, E., Dupuy, R., Colomb, A., Pichon, J. M., Ribeiro, M.,  
950 Bourianne, T., Burnet, F., and Schwarzenboeck, A.: Airborne measurements of new particle  
951 formation in the free troposphere above the Mediterranean Sea during the HYMEX campaign,  
952 *Atmos. Chem. Phys.*, 15, 10203-10218, <https://doi.org/10.5194/acp-15-10203-2015>, 2015.
- 953 Schröder, F. and Ström, J.: Aircraft measurements of sub micrometer aerosol particles ( $> 7$   
954 nm) in the midlatitude free troposphere and tropopause region, *Atmospheric Research*, 44, 333-  
955 356, [https://doi.org/10.1016/S0169-8095\(96\)00034-8](https://doi.org/10.1016/S0169-8095(96)00034-8), 1997.
- 956 Sebastian, M., Kanawade, V. P., Soni, V., Asmi, E., Westervelt, D. M., Vakkari, V., Hyvärinen,  
957 A. P., Pierce, J. R., and Hooda, R. K.: New Particle Formation and Growth to Climate-Relevant  
958 Aerosols at a Background Remote Site in the Western Himalaya, *J. Geophys. Res.*, 126,  
959 e2020JD033267, <https://doi.org/10.1029/2020JD033267>, 2021.
- 960 Sebastian, M., Kompalli, S. K., Kumar, V. A., Jose, S., Babu, S. S., Pandithurai, G., Singh, S.,  
961 Hooda, R. K., Soni, V. K., Pierce, J. R., Vakkari, V., Asmi, E., Westervelt, D. M., Hyvärinen,  
962 A. P., and Kanawade, V. P.: Observations of particle number size distributions and new particle

- 963 formation in six Indian locations, *Atmos. Chem. Phys.*, 22, 4491-4508,  
964 <https://doi.org/10.5194/acp-22-4491-2022>, 2022.
- 965 Sellegri, K., Rose, C., Marinoni, A., Lupi, A., Wiedensohler, A., Andrade, M., Bonasoni, P.,  
966 and Laj, P.: New Particle Formation: A Review of Ground-Based Observations at Mountain  
967 Research Stations, *Atmosphere*, 10, 493, <https://doi.org/10.3390/atmos10090493>, 2019.
- 968 Spracklen, D. V., Carslaw, K. S., Kulmala, M., Kerminen, V.-M., Sihto, S.-L., Riipinen, I.,  
969 Merikanto, J., Mann, G. W., Chipperfield, M. P., Wiedensohler, A., Birmili, W., and  
970 Lihavainen, H.: Contribution of particle formation to global cloud condensation nuclei  
971 concentrations, *Geophys. Res. Lett.*, 35, 2007GL033038,  
972 <https://doi.org/10.1029/2007gl033038>, 2008.
- 973 Stratmann, F., Siebert, H., Spindler, G., Wehner, B., Althausen, D., Heintzenberg, J., Hellmuth,  
974 O., Rinke, R., Schmieder, U., Seidel, C., Tuch, T., Uhrner, U., Wiedensohler, A., Wandinger,  
975 U., Wendisch, M., Schell, D., and Stohl, A.: New-particle formation events in a continental  
976 boundary layer: first results from the SATURN experiment, *Atmos. Chem. Phys.*, 3, 1445-  
977 1459, <https://doi.org/10.5194/acp-3-1445-2003>, 2003.
- 978 Stull, R. B.: An Introduction to Boundary Layer Meteorology, Atmospheric and  
979 Oceanographic Sciences Library, Springer Dordrecht, <https://doi.org/10.1007/978-94-009-3027-8>, 1988.
- 981 Tröstl, J., Herrmann, E., Frege, C., Bianchi, F., Molteni, U., Bukowiecki, N., Hoyle, C. R.,  
982 Steinbacher, M., Weingartner, E., Dommen, J., Gysel, M., and Baltensperger, U.: Contribution  
983 of new particle formation to the total aerosol concentration at the high-altitude site  
984 Jungfraujoch (3580 m asl, Switzerland), *J. Geophys. Res.*, 121, 11,692-611,711,  
985 <https://doi.org/10.1002/2015jd024637>, 2016a.
- 986 Tröstl, J., Chuang, W. K., Gordon, H., Heinritzi, M., Yan, C., Molteni, U., Ahlm, L., Frege, C.,  
987 Bianchi, F., Wagner, R., Simon, M., Lehtipalo, K., Williamson, C. J., Craven, J. S., Duplissy,  
988 J., Adamov, A., Almeida, J., Bernhammer, A. K., Breitenlechner, M., Brilke, S., Dias, A.,  
989 Ehrhart, S., Flagan, R. C., Franchin, A., Fuchs, C., Guida, R., Gysel, M., Hansel, A., Hoyle, C.  
990 R., Jokinen, T., Junninen, H., Kangasluoma, J., Keskinen, H., Kim, J., Krapf, M., Kürten, A.,  
991 Laaksonen, A., Lawler, M. J., Leiminger, M., Mathot, S., Möhler, O., Nieminen, T., Onnela,  
992 A., Petäjä, T., Piel, F. M., Miettinen, P., Rissanen, M. P., Rondo, L., Sarnela, N.,  
993 Schobesberger, S., Sengupta, K., Sipilä, M., Smith, J. N., Steiner, G., Tomè, A., Virtanen, A.,  
994 Wagner, A. C., Weingartner, E., Wimmer, D., Winkler, P. M., Ye, P., Carslaw, K. S., Curtius,  
995 J., Dommen, J., Kirkby, J., Kulmala, M., Riipinen, I., Worsnop, D. R., Donahue, N. M., and  
996 Baltensperger, U.: The role of low-volatility organic compounds in initial particle growth in  
997 the atmosphere, *Nature*, 533, 527-531, <https://doi.org/10.1038/nature18271>, 2016b.
- 998 Vrekoussis, M., Pikridas, M., Rousogenous, C., Christodoulou, A., Desservettaz, M., Sciare,  
999 J., Richter, A., Bougoudis, I., Savvides, C., and Papadopoulos, C.: Local and regional air  
1000 pollution characteristics in Cyprus: A long-term trace gases observations analysis, *Sci. Total*  
1001 *Environ.*, 845, 157315, <https://doi.org/10.1016/j.scitotenv.2022.157315>, 2022.
- 1002 Wang, M. and Penner, J. E.: Aerosol indirect forcing in a global model with particle nucleation,  
1003 *Atmos. Chem. Phys.*, 9, 239-260, <https://doi.org/10.5194/acp-9-239-2009>, 2009.

- 1004 Wehner, B., Werner, F., Ditas, F., Shaw, R. A., Kulmala, M., and Siebert, H.: Observations of  
1005 new particle formation in enhanced UV irradiance zones near cumulus clouds, *Atmos. Chem.*  
1006 *Phys.*, 15, 11701-11711, <https://doi.org/10.5194/acp-15-11701-2015>, 2015.
- 1007 Wehner, B., Siebert, H., Ansmann, A., Ditas, F., Seifert, P., Stratmann, F., Wiedensohler, A.,  
1008 Apituley, A., Shaw, R. A., Manninen, H. E., and Kulmala, M.: Observations of turbulence-  
1009 induced new particle formation in the residual layer, *Atmos. Chem. Phys.*, 10, 4319-4330,  
1010 <https://doi.org/10.5194/acp-10-4319-2010>, 2010.
- 1011 Westervelt, D. M., Pierce, J. R., and Adams, P. J.: Analysis of feedbacks between nucleation  
1012 rate, survival probability and cloud condensation nuclei formation, *Atmos. Chem. Phys.*, 14,  
1013 5577-5597, <https://doi.org/10.5194/acp-14-5577-2014>, 2014.
- 1014 Westervelt, D. M., Pierce, J. R., Riipinen, I., Trivitayanurak, W., Hamed, A., Kulmala, M.,  
1015 Laaksonen, A., Decesari, S., and Adams, P. J.: Formation and growth of nucleated particles  
1016 into cloud condensation nuclei: model-measurement comparison, *Atmos. Chem. Phys.*, 13,  
1017 7645-7663, <https://doi.org/10.5194/acp-13-7645-2013>, 2013.
- 1018 Williamson, C. J., Kupc, A., Axisa, D., Bilsback, K. R., Bui, T., Campuzano-Jost, P., Dollner,  
1019 M., Froyd, K. D., Hodshire, A. L., Jimenez, J. L., Kodros, J. K., Luo, G., Murphy, D. M., Nault,  
1020 B. A., Ray, E. A., Weinzierl, B., Wilson, J. C., Yu, F., Yu, P., Pierce, J. R., and Brock, C. A.:  
1021 A large source of cloud condensation nuclei from new particle formation in the tropics, *Nature*,  
1022 574, 399-403, <https://doi.org/10.1038/s41586-019-1638-9>, 2019.
- 1023 Yu, F. and Luo, G.: Simulation of particle size distribution with a global aerosol model:  
1024 contribution of nucleation to aerosol and CCN number concentrations, *Atmos. Chem. Phys.*, 9,  
1025 7691-7710, <https://doi.org/10.5194/acp-9-7691-2009>, 2009.
- 1026 Zha, Q., Aliaga, D., Krejci, R., Sinclair, V. A., Wu, C., Ciarelli, G., Scholz, W., Heikkinen, L.,  
1027 Partoll, E., Gramlich, Y., Huang, W., Leiminger, M., Enroth, J., Peräkylä, O., Cai, R., Chen,  
1028 X., Koenig, A. M., Velarde, F., Moreno, I., Petäjä, T., Artaxo, P., Laj, P., Hansel, A., Carbone,  
1029 S., Kulmala, M., Andrade, M., Worsnop, D., Mohr, C., and Bianchi, F.: Oxidized organic  
1030 molecules in the tropical free troposphere over Amazonia, *National Science Review*, 11,  
1031 <https://doi.org/10.1093/nsr/nwad138>, 2023.
- 1032 Zhang, D., Comstock, J., and Morris, V.: Comparison of planetary boundary layer height from  
1033 ceilometer with ARM radiosonde data, *Atmos. Meas. Tech.*, 15, 4735-4749,  
1034 <https://doi.org/10.5194/amt-15-4735-2022>, 2022.
- 1035 Zhang, R., Suh, I., Zhao, J., Zhang, D., Fortner, E. C., Tie, X., Molina, L. T., and Molina, M.  
1036 J.: Atmospheric New Particle Formation Enhanced by Organic Acids, *Science*, 304, 1487-  
1037 1490, <https://doi.org/10.1126/science.1095139>, 2004.
- 1038 Zittis, G., Almazroui, M., Alpert, P., Ciais, P., Cramer, W., Dahdal, Y., Fnais, M., Francis, D.,  
1039 Hadjinicolaou, P., Howari, F., Jrrar, A., Kaskaoutis, D. G., Kulmala, M., Lazoglou, G.,  
1040 Mihalopoulos, N., Lin, X., Rudich, Y., Sciare, J., Stenchikov, G., Xoplaki, E., and Lelieveld,  
1041 J.: Climate Change and Weather Extremes in the Eastern Mediterranean and Middle East, *Rev.*  
1042 *Geophys.*, 60, e2021RG000762, <https://doi.org/10.1029/2021R, G000762>, 2022.